High-Contrast *In Vivo* Imaging of Tau Pathologies in Alzheimer's and Non-Alzheimer's Disease Tauopathies

Highlights

- A new probe, PM-PBB3, captures pathological tau deposits *in vivo* with high contrast

- PM-PBB3 allows an individual-based identification of AD and non-AD tauopathies

- Autopsy assays of PET-scanned patients supported the *in vivo* performance of PM-PBB3

Authors

Kenji Tagai, Maiko Ono, Manabu Kubota, ..., Naruhiko Sahara, Makoto Higuchi, Hitoshi Shimada

Correspondence

takado.yuhei@qst.go.jp (Y.T.),
higuchi.makoto@qst.go.jp (M.H.)

In Brief

Tagai et al. developed a positron emission tomography probe, ^{18}F-PM-PBB3, for tau deposits in Alzheimer's and non-Alzheimer's disease tauopathies. This probe was demonstrated to enable individual- and pathology-based diagnosis, differentiation, and staging of these disorders in addition to translational research and development on tauopathies from mouse models to humans.

Neuron

Article

High-Contrast *In Vivo* Imaging of Tau Pathologies in Alzheimer's and Non-Alzheimer's Disease Tauopathies

Kenji Tagai,[1,2,17] Maiko Ono,[1,17] Manabu Kubota,[1,3,17] Soichiro Kitamura,[1,4] Keisuke Takahata,[1,5] Chie Seki,[1] Yuhei Takado,[1,*] Hitoshi Shinotoh,[1,6] Yasunori Sano,[1,5] Yasuharu Yamamoto,[1,5] Kiwamu Matsuoka,[1,4] Hiroyuki Takuwa,[1] Masafumi Shimojo,[1] Manami Takahashi,[1] Kazunori Kawamura,[1] Tatsuya Kikuchi,[1] Maki Okada,[1] Haruhiko Akiyama,[7] Hisaomi Suzuki,[1,5,8] Mitsumoto Onaya,[8] Takahiro Takeda,[9] Kimihito Arai,[9] Nobutaka Arai,[10] Nobuyuki Araki,[9] Yuko Saito,[11] John Q. Trojanowski,[12] Virginia M.Y. Lee,[12] Sushil K. Mishra,[13] Yoshiki Yamaguchi,[14] Yasuyuki Kimura,[1,15] Masanori Ichise,[1] Yutaka Tomita,[16] Ming-Rong Zhang,[1] Tetsuya Suhara,[1,2] Masahiro Shigeta,[2] Naruhiko Sahara,[1] Makoto Higuchi,[1,18,*] and Hitoshi Shimada[1]

[1]National Institute of Radiological Sciences, National Institutes for Quantum and Radiological Science and Technology, Chiba 263-8555, Japan
[2]Department of Psychiatry, The Jikei University Graduate School of Medicine, Tokyo 105-8461, Japan
[3]Department of Psychiatry, Kyoto University Graduate School of Medicine, Kyoto 606-8507, Japan
[4]Department of Psychiatry, Nara Medical University, Nara 634-8521, Japan
[5]Department of Psychiatry, Keio University School of Medicine, Tokyo 160-0016, Japan
[6]Neurology Clinic Chiba, Chiba 263-8555, Japan
[7]Dementia Research Project, Tokyo Metropolitan Institute of Medical Science, Tokyo 156-8506, Japan
[8]National Hospital Organization Shimofusa Psychiatric Medical Center, Chiba 266-0007, Japan
[9]Department of Neurology, National Hospital Organization Chibahigashi National Hospital, Chiba 260-8712, Japan
[10]Laboratory of Neuropathology, Tokyo Metropolitan Institute of Medical Science, Tokyo 156-8506, Japan
[11]National Center of Neurology and Pathology Brain Bank, National Center Hospital, National Center of Neurology and Psychiatry, Tokyo 187-8551, Japan
[12]Center for Neurodegenerative Disease Research and Institute on Aging, Perelman School of Medicine, University of Pennsylvania, Philadelphia, PA 19104, USA
[13]Glycoscience Group, National University of Ireland, Galway H91 W2TY, Ireland
[14]Laboratory of Pharmaceutical Physical Chemistry, Tohoku Medical and Pharmaceutical University, Miyagi 981-8558, Japan
[15]Department of Clinical and Experimental Neuroimaging, Center for Development of Advanced Medicine for Dementia, National Center for Geriatrics and Gerontology, Aichi 474-8511, Japan
[16]Tomita Hospital, Aichi 444-3505, Japan
[17]These authors contributed equally
[18]Lead Contact
*Correspondence: takado.yuhei@qst.go.jp (Y.T.), higuchi.makoto@qst.go.jp (M.H.)
https://doi.org/10.1016/j.neuron.2020.09.042

SUMMARY

A panel of radiochemicals has enabled *in vivo* positron emission tomography (PET) of tau pathologies in Alzheimer's disease (AD), although sensitive detection of frontotemporal lobar degeneration (FTLD) tau inclusions has been unsuccessful. Here, we generated an imaging probe, PM-PBB3, for capturing diverse tau deposits. *In vitro* assays demonstrated the reactivity of this compound with tau pathologies in AD and FTLD. We could also utilize PM-PBB3 for optical/PET imaging of a living murine tauopathy model. A subsequent clinical PET study revealed increased binding of ^{18}F-PM-PBB3 in diseased patients, reflecting cortical-dominant AD and subcortical-dominant progressive supranuclear palsy (PSP) tau topologies. Notably, the *in vivo* reactivity of ^{18}F-PM-PBB3 with FTLD tau inclusion was strongly supported by neuropathological examinations of brains derived from Pick's disease, PSP, and corticobasal degeneration patients who underwent PET scans. Finally, visual inspection of ^{18}F-PM-PBB3-PET images was indicated to facilitate individually based identification of diverse clinical phenotypes of FTLD on a neuropathological basis.

INTRODUCTION

The vast majority of age-related neurodegenerative diseases are characterized as protein conformational disorders, which involve self-assemblies of misfolded proteins into fibrillary aggregates (Soto and Pritzkow, 2018; Walker and Jucker, 2015). Among these pathogenic proteins, the fibrillogenesis of microtubule-associated protein tau occurs as a hallmark pathological change

in diverse illnesses referred to as tauopathies, and it is mechanistically linked to the neurodegenerative processes in these disorders (Iqbal et al., 2016; Spillantini and Goedert, 2013). Tau in the central nervous system is composed of six isoforms, which are classified into three- and four-repeat species according to the number of repeat domains (Buée et al., 2000). Alzheimer's disease (AD) and AD-type primary age-related tauopathy (PART) are characterized by tau pathologies formed by all isoforms, although a significant subset of frontotemporal lobar degeneration (FTLD) syndromes is neuropathologically unfolded by exclusive fibrillization of either three- or four-repeat tau isoforms (Buée et al., 2000; Lee et al., 2001).

The distinct tau conformers are likely to determine subcellular, cellular, and regional localization of tau deposits in a disease-specific fashion, provoking characteristic symptoms associated with deteriorations of affected neurons and neural circuits (Forrest et al., 2019). In line with this mechanism, there exist clear distinctions among neuropathological features of AD/PART and major tau-positive FTLD disorders, including three-repeat tauopathies represented by Pick's disease (PiD) and four-repeat tauopathies exemplified by progressive supranuclear palsy (PSP) and corticobasal degeneration (CBD) (Lee et al., 2001). Meanwhile, substantial overlaps have been noted among symptomatic phenotypes derived from these pathologies, impeding the differentiation of clinical syndromes by estimation of underlying pathological alterations (Rabinovici and Miller, 2010; Williams and Lees, 2009; Zhang et al., 2020).

In vivo imaging technologies, such as positron emission tomography (PET) with specific radioligands for amyloid-beta and tau fibrils, have enabled visualization of AD-type neuropathologies in living subjects, facilitating diagnosis and staging of AD dementia and its prodrome. The tau PET probes available for these clinical assays are classified into three chemotypes consisting of ^{18}F-labeled THK5351 (Harada et al., 2016), ^{18}F-labeled flortaucipir (Chien et al., 2014), and ^{11}C-labeled PBB3 (Maruyama et al., 2013; Shimada et al., 2016) series. Unlike for AD tau lesions, high-contrast PET detection of three- and four-repeat tau deposits in FTLD patients has been controversial. Tau-related radiosignals yielded by ^{18}F-flortaucipir and ^{11}C-PBB3 in PSP and CBD cases were less than 20% of the corresponding signals in patients with advanced AD (Endo et al., 2019; Schonhaut et al., 2017). ^{18}F-THK5351 was reported to illuminate brain areas putatively enriched with PSP and CBD tau inclusions (Brendel et al., 2018; Kikuchi et al., 2016). However, those observations were attributed to the cross-reactivity of this compound with monoamine oxidase B (MAO-B), which is upregulated in reactive astrocytes (Harada et al., 2018; Ng et al., 2017). In addition, most "second-generation" tau PET probes are analogs of ^{18}F-fluotaucipir and are not overtly more reactive with non-AD tau assemblies than ^{18}F-fluotaucipir and ^{11}C-PBB3 (Aguero et al., 2019; Honer et al., 2018). Among these radiotracers, an ^{18}F-flortaucipir analog, ^{18}F-PI-2620, was reported to show promising characteristics as an imaging agent for PSP tau aggregates in a non-clinical study (Kroth et al., 2019), although the *in vivo* performance of this radioligand for the differentiation of PSP subjects from controls has not markedly exceeded that of ^{18}F-flortaucipir (Brendel et al., 2020).

[11]C-PBB3 was originally designed to capture tau fibrils in a wide range of tauopathies (Maruyama et al., 2013) and was demonstrated to react with three- and four-repeat tau aggregates in human brain tissues with a higher binding potential than ^{18}F-flortaucipir (Ono et al., 2017). However, rapid conversion of ^{11}C-PBB3 into a metabolite resulted in a relatively low entry of the unmetabolized compound into the brain (Hashimoto et al., 2014; Kimura et al., 2015; Maruyama et al., 2013), hampering a sensitive recognition of fibrillary aggregates in FTLD tauopathies that are less abundant than AD tau deposits. To overcome this technical issue, in the current work, we modified the chemical structure of PBB3 to generate a chemical with a relatively high metabolic stability, aiming at unambiguous investigations of tau fibril density and extent in each of the individuals with AD and FTLD. The new compound, PM-PBB3 (propanol modification of PBB3), was fluorinated in consideration of the advantages of an ^{18}F-labeled probe over ^{11}C-radiochemicals for broader availability and higher PET scan throughput. Nonclinical assays revealed the capability of PM-PBB3 for high-sensitivity illumination of tau pathologies in a murine model bimodally by *in vivo* optical and PET imaging from single-cell to brain-wide scales, potentially serving for the discovery of candidate therapeutics counteracting the neurodegenerative tau pathogenesis. Subsequent applications of ^{18}F-PM-PBB3 to clinical PET assays, along with neuropathological data obtained from scanned subjects, demonstrated appropriate kinetic and binding profiles of this probe for personalized evaluations of tau depositions in AD and various FTLD syndromes.

RESULTS

In Vitro Binding of PM-PBB3 to AD- and FTLD-type Tau Aggregates

The original compound, PBB3 (Figure 1A), was found to be promptly conjugated with sulfate at a hydroxy moiety following systemic injection (Hashimoto et al., 2015). To suppress this metabolic conversion, we substituted this substructure with the fluoro-isopropanol group, resulting in the generation of PM-PBB3 (Figure 1A). This modification allowed ^{18}F radiolabeling of the probe using a tosylate precursor (Figure S1), and the strong binding of PM-PBB3 to a non-AD tau filament was supported by a molecular dynamics simulation based on ultrastructures of tau assemblies determined by cryo-electron microscope (Figure S2). Similar to PBB3 (Maruyama et al., 2013; Ono et al., 2017), PM-PBB3 is self-fluorescent, and its reactivity with pathological tau fibrils is assessable by fluorescence labeling of brain sections derived from tauopathy patients. Triple staining of brain slices with PM-PBB3, antibody against phosphorylated tau (AT8), and Gallyas-Braak silver impregnation (GB) demonstrated binding of PM-PBB3 to tau lesions in AD hippocampal formation, which were composed of six tau isoforms (Figure 1B). Furthermore, PM-PBB3 conspicuously illuminated Pick bodies constituted of three-repeat tau isoforms in PiD frontal cortex and four-repeat tau lesions in striatum of PSP and CBD (Figure 1B).

We then radiosynthesized ^{18}F-PM-PBB3 and examined its *in vitro* binding characteristics. Autoradiography of tissue sections demonstrated that ^{18}F-PM-PBB3 radiosignals were intensely distributed in the anatomical structures enriched with
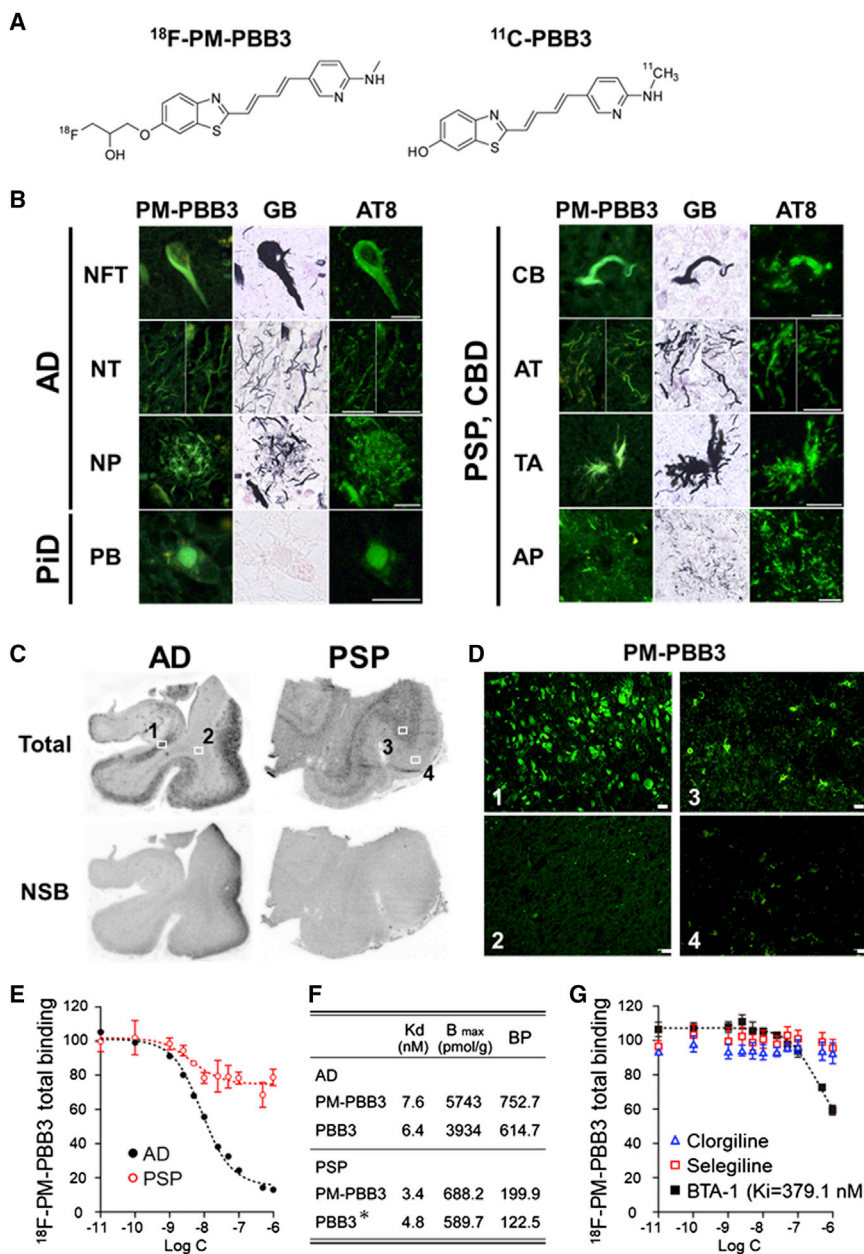
Figure 1. *In Vitro* Binding of PM-PBB3 to Tau Lesions in AD, PiD, PSP, and CBD

(A) Chemical structural formulae of ^{18}F-PM-PBB3 (left) and ^{11}C-PBB3 (right).

(B) Triple staining of tau lesions in the hippocampal formation of an AD patient (AD-1, also see Table S4, left composite), the frontal cortex of a PiD patient (PiD-1, left composite), and the caudate/putamen of PSP and CBD patients (PSP-1 and CBD-1, right composite) with 25 μM of non-radiolabeled PM-PBB3, GB, and AT8. NFTs, neuropil threads (NTs), and dystrophic neurites encompassing a neuritic plaque (NP) in AD brain sections; pick body (PB) in PiD brain section; and coiled body (CB), argyrophilic threads (ATs), tufted astrocyte (TA), and astrocytic plaque (AP) in PSP/CBD brain sections are clearly labeled with PM-PBB3. Scale bars, 20 μm.

(C) Autoradiographic labeling of AD brain sections, including the hippocampal formation and inferior temporal cortex (AD-2, left) and a PSP motor cortex section (PSP-2, right) with 5 nM of ^{18}F-PM-PBB3 in the absence (top, total binding) and presence (bottom, non-specific binding [NSB]) of 100 μM of non-radiolabeled PBB5, an analog of PM-PBB3.

(D) Photomicrographs of fluorescence staining with PM-PBB3 in areas indicated by squares in (C). In line with autoradiographic data, NFTs and neuropil threads in the AD subiculum (1) and coiled bodies and tufted astrocytes in middle gray matter layers of the PSP motor cortex (3) were intensely labeled with 25 μM of non-radiolabeled PM-PBB3, in contrast with the lack of overt fluorescence signals in the white matter of the AD temporal cortex (2) and superficial gray matter layers of the PSP motor cortex (4). Scale bars, 20 μm.

(E) Total (specific + non-specific) bindings of 1 nM of ^{18}F-PM-PBB3 in AD frontal cortex (AD-3, closed circles) and PSP motor cortex (PSP-2, open circles) samples were homologously blocked by non-radiolabeled PM-PBB3 in a concentration-dependent fashion, indicating binding saturability, and a one-site binding model was employed for describing the inhibition plots. Data are mean values ± SD in four samples and are expressed as % of averaged total binding.

(F) Binding parameters for ^{18}F-PM-PBB3 determined by non-linear fitting of a one-site homologous blockade model to the data shown in (E) and binding parameters for ^{11}C-PBB3 in AD frontal cortex and PSP motor cortex samples. Data are adopted from Ono et al. (2017).

(G) Inhibition of total binding of 1 nM of ^{18}F-PM-PBB3 by clorgiline (MAO-A inhibitor, blue triangle), selegiline (MAO-B inhibitor, red square), and BTA-1 (analog of PiB, black square) in an AD frontal cortex sample (AD-3). A part of ^{18}F-PM-PBB3 total binding was heterologously blocked by BTA-1 with relatively large Ki (379.1 nM). Total binding of ^{18}F-PM-PBB3 was not inhibited by clorgiline and selegiline at varying concentrations, and Ki for clorgiline and selegiline was not determined due to failures of the model fitting. Data are mean values ± SD in four samples and are expressed as % of the averaged total binding.

AD and PSP tau fibrils (Figure 1C). Localization of the autoradiographic labeling was in line with histological features obtained from the same sections, as abundant neurofibrillary tangles (NFTs) and neuropil threads in the AD subiculum, and coiled bodies and tufted astrocytes in middle gray matter layers of the PSP motor cortex were captured by non-radiolabeled PM-PBB3 (areas 1 and 3 in Figure 1D). In contrast, the lack of overt autoradiographic radioligand binding spatially agreed with minimal PM-PBB3 fluorescence in white matter of the AD temporal cortex and in superficial gray matter layers of the PSP motor cortex (areas 2 and 4 in Figure 1D).

We also quantified the affinity of ^{18}F-PM-PBB3 for tau aggregates in homogenized AD frontal cortical and PSP motor cortical tissues (Figure 1E). ^{18}F-PM-PBB3 displayed high-affinity, high-capacity binding in AD homogenates (dissociation constant [K_D], 7.63 nM; concentration of binding components [B_{max}], 5,743
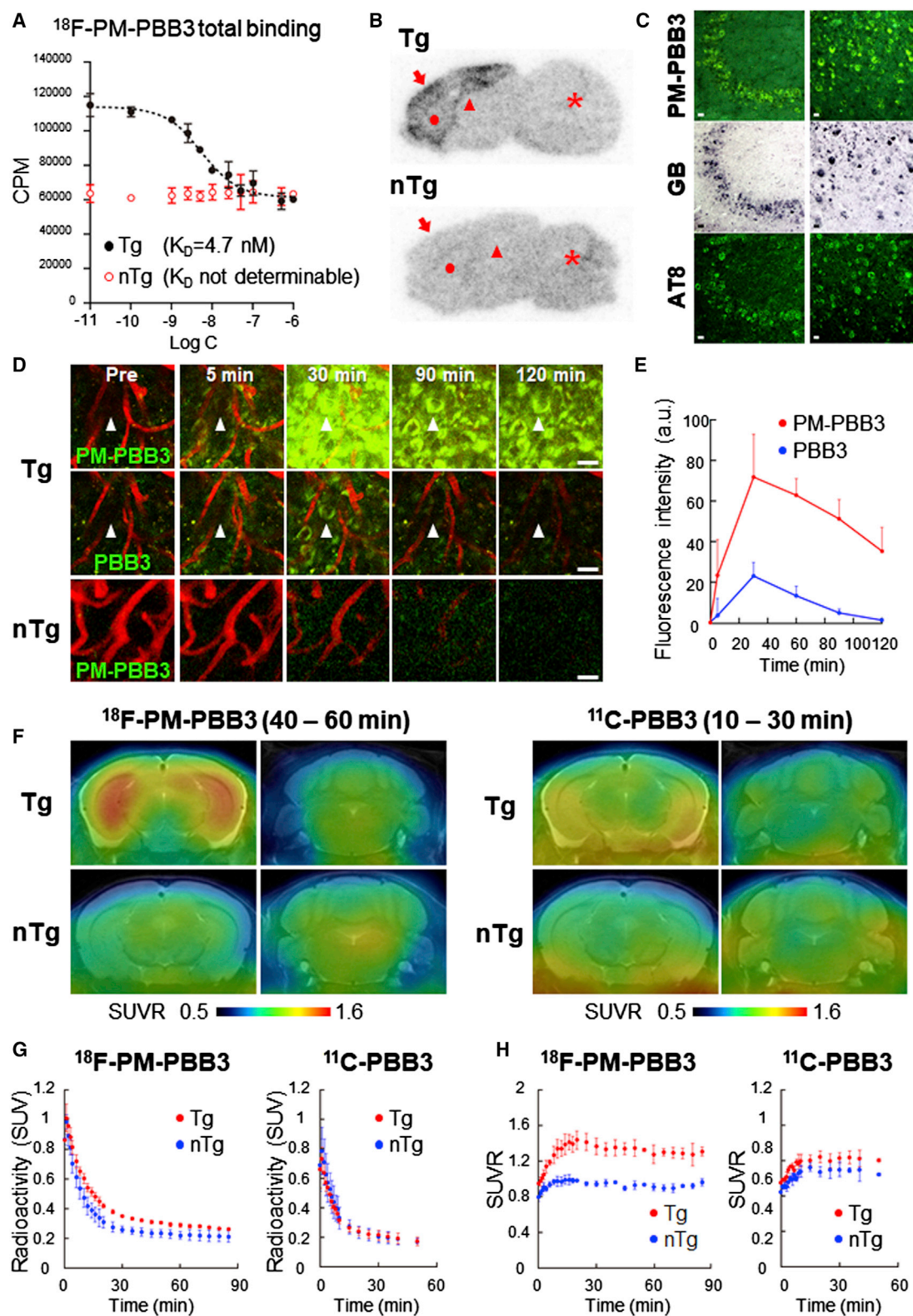
pmol/g; binding potential [BP = B$_{max}$/K$_D$], 752.7; Figure 1F). The radioligand bound in PSP tissues with lower capacity but higher affinity than in AD tissues (K$_D$, 3.44 nM; B$_{max}$, 688.2 pmol/g; BP, 199.9). The BPs for ^{18}F-PM-PBB3 were 1.2 and 1.6 times higher than the values for ^{11}C-PBB3 in the same AD and PSP homogenate samples, respectively (Figure 1F). The binding of ^{18}F-PM-PBB3 in AD homogenates was partially and heterologously blocked by BTA-1, which is a Pittsburgh Compound-B (PiB) analog and binds to Aβ aggregates with high affinity, with a large inhibition constant (Ki) value (379.1 nM; Figure 1G), suggesting that ^{18}F-PM-PBB3 is incapable of sensitively capturing Aβ deposits in AD homogenates (Klunk et al., 2001; Ni et al., 2018). Moreover, the heterologous blockade by BTA-1 is likely to stem primarily from its low-affinity binding to AD tau fibrils (Klunk et al., 2001; Ni et al., 2018). Notably, minimal displacement of ^{18}F-PM-PBB3 binding was observed in the presence of the monoamine oxidase A (MAO-A) inhibitor clorgiline, or the MAO-B inhibitor selegiline, in AD frontal cortex homogenates (Figure 1G), suggesting that ^{18}F-PM-PBB3 barely cross-reacts with off-target binding sites on monoamine oxidases, unlike the reported binding of ^{18}F-THK5351 and ^{18}F-flortaucipir to MAO-B (Harada et al., 2018; Lemoine et al., 2018; Ng et al., 2017) and/or MAO-A (Vermeiren et al., 2018).

Optical and PET Detection of Tau Deposits in Living Tauopathy Model Mice

For assessing *in vivo* interactions of PM-PBB3 with intracellular tau deposits, we utilized a murine transgenic (Tg) model of tauopathies dubbed rTg4510, which overexpresses a human four-repeat tau isoform with the P301L mutation causative of familial FTLD (Sahara et al., 2014; Santacruz et al., 2005). ^{18}F-PM-PBB3 bound to tau fibrils in homogenized forebrain tissues obtained from Tg with high affinity, although there was no homologously displaceable radioligand binding in non-transgenic (nTg) forebrain homogenates (Figure 2A). The BP for ^{18}F-PM-PBB3 was 1.5-fold higher than the value for ^{11}C-PBB3 in the same Tg samples (Figure S3). *Ex vivo* autoradiography of brain tissues collected from mice demonstrated accumulations of ^{18}F-PM-PBB3 in the Tg forebrain harboring neuronal tau inclusions (Figure 2B). Conversely, there was no noticeable increase of ^{18}F-PM-PBB3 retentions in the nTg forebrain (Figure 2B). Triple staining of brain sections used for *ex vivo* autoradiography with PM-PBB3 fluorescence, GB, and AT8 illustrated strong binding of PM-PBB3 to intracellular tau aggregates in the hippocampus and neocortex of a Tg mouse (Figure 2C).

To assess the time course of *in vivo* labeling of intraneuronal tau aggregates with PM-PBB3, we conducted intravital two-photon laser fluorescence microscopy with a cranial window to the somatosensory cortex of the Tg and nTg mice. Comparison of PM-PBB3 and PBB3 signals in the same field of view indicated rapid entry of these probes into the brain after intravenous probe administration, reaching tau aggregates within 5 min (Figure 2D). Quantification of the background-corrected fluorescence intensity revealed that PM-PBB3 yielded 3-fold higher peak fluorescence signals in the same neurons burdened with tau aggregate than PBB3 (Figure 2E). In contrast, no noticeable increases in fluorescence signals were produced by intravenously injected PM-PBB3 in neurons of nTg mice (Figure 2D).

The *in vivo* performance of ^{18}F-PM-PBB3 and ^{11}C-PBB3 as a PET probe was then examined by a head-to-head comparison in the same mice (Figures 2F–2H). ^{18}F-PM-PBB3 rapidly entered the brain after intravenous administration, and the peak radioactivity uptake was 1.4-fold higher than that of ^{11}C-PBB3 (Figure 2G). This was followed by a prompt washout of radioactivity

Figure 2. *In Vivo* Performances of PM-PBB3 as a Multimodal Probe for Optical and PET Imaging of Tau Aggregates in a Transgenic Mouse Model

(A) Total (specific + non-specific) bindings of 1 nM of ^{18}F-PM-PBB3 in forebrain samples obtained from 21-month-old male rTg4510 transgenic (Tg) (closed circles) and non-transgenic (nTg) (open circles) mice were homologously blocked by non-radiolabeled PM-PBB3 with varying concentrations, and a one-site binding model was employed for describing the inhibition plots. Data are mean values ± SD in four samples and are expressed as cpm.

(B) *Ex vivo* autoradiographic labeling with intravenously injected ^{18}F-PM-PBB3 in 9.7-month-old female Tg (top) and male nTg (bottom) control mice. The brains were removed at 30 min after injection and were cut into sagittal slices. Significant accumulation of ^{18}F-PM-PBB3 was observed in the hippocampus (arrowhead), neocortex (arrow), and striatum (circle) of a Tg mouse. On the other hand, no significant accumulation of ^{18}F-PM-PBB3 showed in these brain areas of a nTg mouse. In addition, the radioligand accumulation was minimal in the Tg and nTg cerebellums, which were devoid of tau pathologies (asterisks).

(C) *Post mortem* triple staining of Tg brain sections used in *ex vivo* autoradiographic experiment with 25 μM of non-radiolabeled PM-PBB3, GB, and AT8. Numerous intracellular deposits in the hippocampal (left) and neocortical (right) areas corresponding to portions indicated by arrowhead and arrow, respectively, in (B) were strongly labeled with PM-PBB3, GB, and AT8. Scale bars, 20 μm.

(D) *In vivo* two-photon laser microscopic images showing a maximum intensity projection of fluorescence signals in a 3D volume of the somatosensory cortex of 8-month-old male Tg (top and middle) and nTg (bottom) mice. Cerebral blood vessels were labeled in red with intraperitoneally administered sulforhodamine 101, and tau aggregates in the Tg mouse were illuminated in green with intravenously injected non-radiolabeled PM-PBB3 (top) or PBB3 (middle), in contrast to minimal retentions of PM-PBB3 in the nTg mouse brain (bottom). Images were acquired before (pre) and 5, 30, 90, and 120 min after the tracer administration. Arrowheads denote the same tau inclusion detected by PM-PBB3 and PBB3. Scale bars, 20 μm.

(E) Chronological changes of fluorescence signals derived from PM-PBB3 (red circles) and PBB3 (blue circles) in identical neurons bearing tau aggregate in the somatosensory cortex of Tg mouse over 120 min after the tracer administration in *in vivo* two-photon microscopic imaging. Fluorescence signal intensities normalized accordingly to the background signals were expressed as arbitrary units (a.u.), and data are mean values ± SD in 10 neurons.

(F) Coronal brain images of 9-month-old female Tg (top) and nTg (bottom) mice acquired by averaging dynamic PET data at 40–60 and 10–30 min after intravenous administration of ^{18}F-PM-PBB3 (left composite) and ^{11}C-PBB3 (right composite), respectively. Brain volume data were sectioned at 3 mm (left column in each composite) and 6 mm (right column in each composite) posterior to the bregma to generate images containing the neocortex/hippocampus and cerebellum/brainstem, respectively. PET images are superimposed on individual MRI data, and voxel values represent the SUVR generated using the cerebellum as reference region for each radiotracer.

(G and H) Time-radioactivity curves (G; SUV) and ratio of the radioactivity uptake to the cerebellum (H; SUVR) in the hippocampus of 8- to 9-month-old female Tg (red circles) and nTg (blue circles) mice over 90 and 60 min after intravenous injection of ^{18}F-PM-PBB3 (left) and ^{11}C-PBB3 (right). Data are mean ± SD in three Tg or nTg animals, and the same individuals were used for a head-to-head comparison of the two radiotracers.

Radiotracer binding (SUVR)
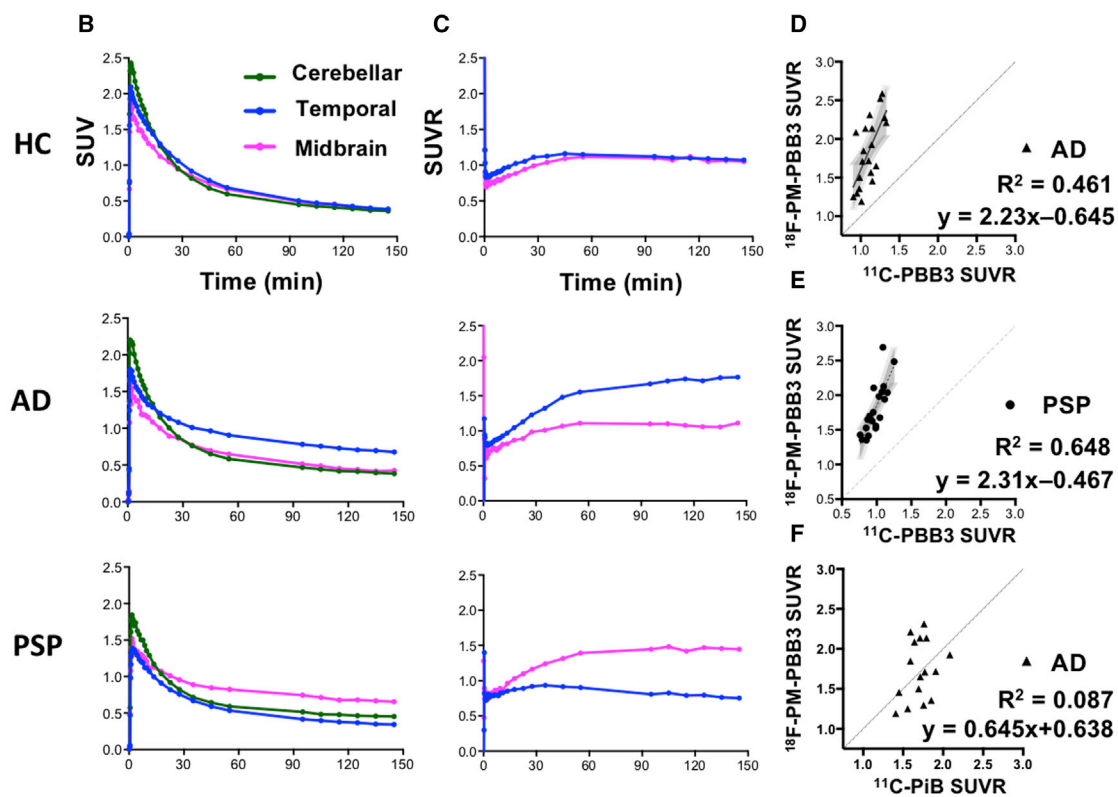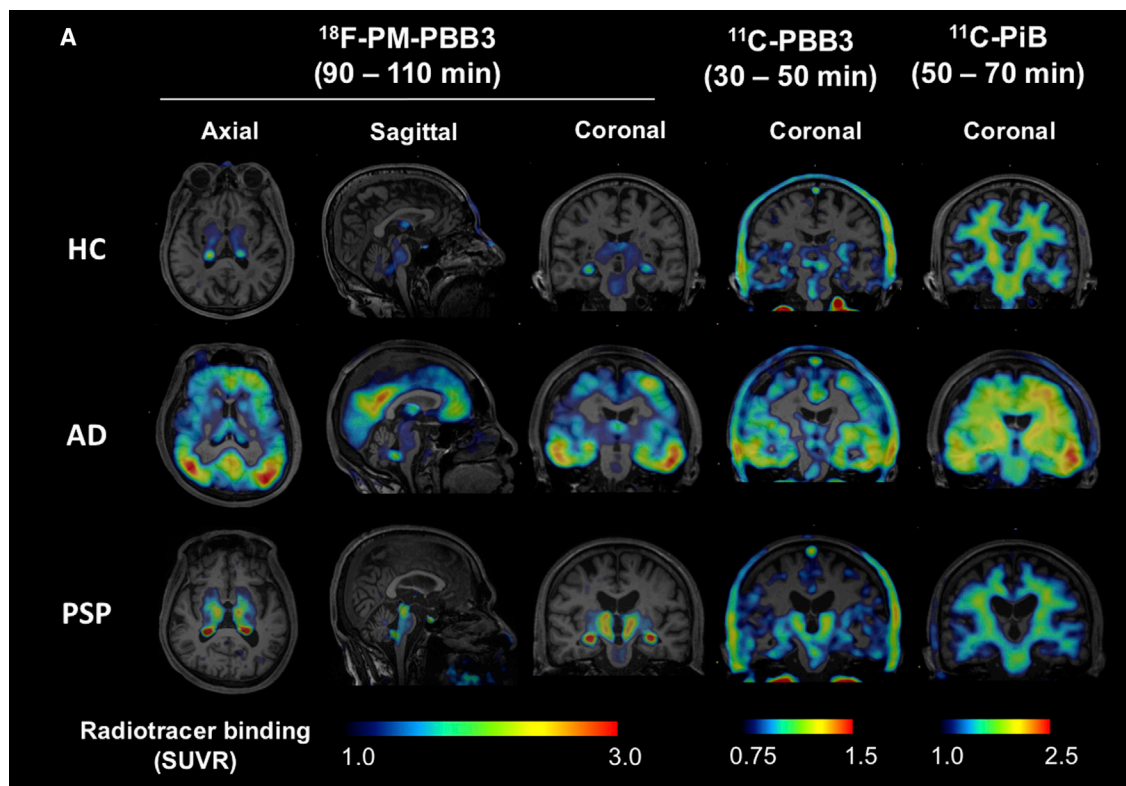
from the brains of nTg mice, whereas the clearance was retarded in the Tg forebrain, reflecting radioligand binding to tau deposits. ^{18}F-PM-PBB3 generated a more than 2-fold higher contrast for tau lesions in the Tg hippocampus relative to nTg controls than ^{11}C-PBB3 (Figure 2H).

The high brain uptake and tau contrast by ^{18}F-PM-PBB3 versus ^{11}C-PBB3 were partly attributable to its stability against bio-metabolism (Table S1). ^{18}F-PM-PBB3 has been confirmed to be decomposed to a hydrophilic radiometabolite in human plasma at a slower rate than metabolizing ^{11}C-PBB3 (Figures S4A and S4B).

High-Contrast PET Imaging of AD and PSP Tau Pathologies in Humans Enabled by ^{18}F-PM-PBB3

Encouraged by non-clinical results, ^{18}F-PM-PBB3 was applied to PET imaging in human subjects. As depicted in Figure 3A, the retention of ^{18}F-PM-PBB3 clearly visualized the neocortical and limbic dominance of six tau isoform accumulations in an AD patient and subcortical dominance of four-repeat tau depositions in a PSP patient with Richardson's syndrome (PSP-Richardson), a PSP subcategory with a typical clinical phenotype (Höglinger et al., 2017), in sharp contrast to the low radiosignals sustained in the parenchyma of elderly healthy control (HC) brains (Figure 3A).

The uptake of ^{18}F-PM-PBB3 peaked rapidly after radioligand injection and subsequently declined by more than 50% across all regions of the HC brain in the next 30 min, resulting in uniformly low radioligand retention (Figure 3B). The clearance of ^{18}F-PM-PBB3 was profoundly slowed in tau-burdened areas of the AD and PSP brains, conceivably reflecting the specific radioligand binding to tau aggregates (Figure 3B). The cerebellum was included in brain areas with the lowest radioactivity retention (Figure 3B), supporting the use of cerebellar gray matter as a reference tissue with a minimal tau fibril load for quantification of the radioligand binding. The target-to-reference ratio of the radioactivity (standardized uptake value ratio [SUVR]) was progressively increased in affected brain areas until ~60 min after radioligand injection, and then, it almost plateaued at ~90 min (Figure 3C).

In subjects who underwent arterial blood sampling during the PET scan, full kinetic analyses showed that mathematical models with a single input function could robustly quantify the tracer binding (Figures S4C–S4E; Table S2). Distribution volume ratio (DVR) also displayed an excellent correlation to SUVR values determined from 20-min scan data obtained from 90 min or later after the radioligand injection in HCs and AD patients ($r > 0.987$) and in PSP patients ($r > 0.992$; Figures S5A and

S5B). Therefore, we choose the earliest time frame, 90–110 min, for the most practical scan protocol. A simulation analysis also demonstrated that ^{18}F-PM-PBB3 binding measures are insensitive to regional and global cerebral blood flow alterations (Figures S6A–S6C).

To examine the superiority of ^{18}F-PM-PBB3 over ^{11}C-PBB3 as a high-sensitivity tau PET probe, we carried out a head-to-head comparison of PET data with these radioligands in the same individuals. The peak uptake of ^{18}F-PM-PBB3 in the brain (Figure 3B) was approximately 2-fold higher than that of ^{11}C-PBB3 (Maruyama et al., 2013), and non-specific radioactivity retentions in the basal ganglia and venous sinuses at high levels and several neocortical areas at low levels were provoked in a HC subject by ^{11}C-PBB3, but not ^{18}F-PM-PBB3 (Figure 3A). Meanwhile, radioactivity accumulations in the choroid plexus, which were documented in the use of other tau radioligands, including ^{18}F-flortaucipir (Ikonomovic et al., 2016; Lee et al., 2018; Lowe et al., 2016), were augmented in ^{18}F-PM-PBB3-PET images as compared to PET data with ^{11}C-PBB3 (Figure 3A). The linear regression slopes in a scatterplot of ^{18}F-PM-PBB3 versus ^{11}C-PBB3 binding indicated that ^{18}F-PM-PBB3 produced more than 2-fold higher contrasts for AD and PSP tau deposits than ^{11}C-PBB3 (Figures 3D and 3E).

As there was no significant correlation between SUVRs for ^{18}F-PM-PBB3 and ^{11}C-PiB in AD patients ($r = 0.295$; $p = 0.268$; Figure 3F), it is unlikely that PET data with ^{18}F-PM-PBB3 can be considerably affected by its cross-reactivity with Aβ deposits.

The Utility of ^{18}F-PM-PBB3 for PET Assessments of the Topology and Stage of AD-Spectrum and PSP Tau Pathologies

We performed tau and Aβ PET scans with ^{18}F-PM-PBB3 and ^{11}C-PiB, respectively, for three mild cognitive impairment (MCI) and 14 AD patients (mean age ± SD, 70.7 ± 11.9 years) as well as 23 HCs (mean age ± SD, 65.2 ± 7.9 years) in order to investigate the ability of ^{18}F-PM-PBB3 to capture the advancement of AD-spectrum tau pathologies in each individual. To this aim, we defined composite voxels of interest (VOIs) according to Braak's NFT stages (Figure S7; Cho et al., 2016; Schöll et al., 2016). All HCs were negative for ^{11}C-PiB-PET, and all MCI and AD patients were positive for ^{11}C-PiB-PET, based on visual inspection of the acquired images. Representative ^{18}F-PM-PBB3-PET images demonstrated expansions of radiosignals from the medial temporal cortex to the other neocortical and limbic areas, along with progression of the NFT stage (Figures 4A and 4B). ^{18}F-PM-PBB3 SUVRs in stage I/II VOI were elevated in a subset of HCs, being overlapped with the values in MCI and AD patients,

Figure 3. AD and PSP Tau Topologies Visualized with High Contrast by PET with ^{18}F-PM-PBB3 as Compared to ^{11}C-PBB3 in the Same Human Subjects

(A) Orthogonal ^{18}F-PM-PBB3 and coronal ^{11}C-PBB3 and ^{11}C-PiB-PET images in the same HC and AD and PSP patients. Images of the PSP patient were derived from an autopsy-confirmed PSP case. Data are displayed as parametric maps for radioligand SUVR. Non-thresholded ^{18}F-PM-PBB3 images are also shown in Figure S11.

(B and C) Time course changes of the radioligand uptake (B; %SUV) and SUVR to the cerebellum (C) in the cerebellum (green), temporal cortex (blue), and midbrain (magenta) of representative HC and AD and PSP patients over 150 min after intravenous injection of ^{18}F-PM-PBB3.

(D–F) Scatterplots demonstrating head-to-head comparisons of SUVR values between ^{18}F-PM-PBB3 and ^{11}C-PBB3 in the AD (D) and PSP (E) brains and between ^{18}F-PM-PBB3 and ^{11}C-PiB in the AD brain (F). Significant regression results are also shown. SUVR values were generated from four VOIs in each patient (see Figure S7 for the VOI definition).
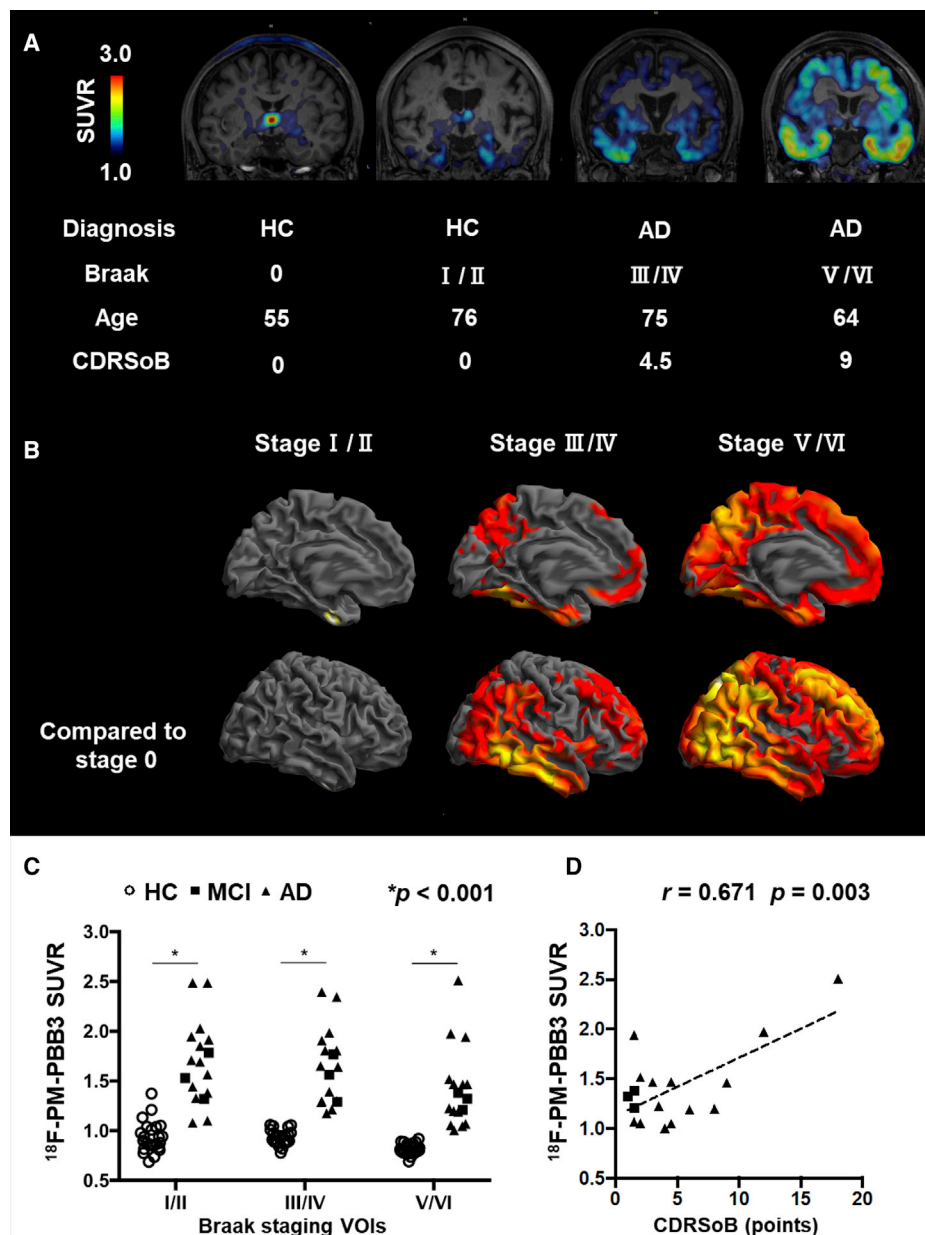
Figure 4. Associations between the Clinical Disease Severity and the Extent of Areas Showing Increased ^{18}F-PM-PBB3 Binding in the AD Spectrum

(A) Coronal ^{18}F-PM-PBB3-PET images of HCs and AD patients classified into different Braak tau stages.

(B) The topology of increased ^{18}F-PM-PBB3 binding in subjects at each Braak stage compared to 22 HCs (stage zero). p < 0.005, uncorrected, for one HC (stage I/II); p < 0.05, familywise error corrected at cluster level, for four MCI/AD patients (stage III/IV) and for 13 MCI/AD patients (stage V/VI).

(C) Comparisons of ^{18}F-PM-PBB3 binding in Braak stage VOIs between 23 HCs (white circles) and three MCI (black squares) and 14 AD (black triangles) cases. *p < 0.001 by two-sample t test.

(D) Correlation of ^{18}F-PM-PBB3 binding in the Braak stage V/VI VOI with CDRSoB points in MCI (black squares) and AD (black triangles) patients. $r = 0.671$ and $p = 0.003$ by Pearson's correlation analysis. Associations between the clinical disease severity and the extension of ^{18}F-PM-PBB3 binding among MCI/AD patients.

and this may imply accumulations of tau fibrils in the medial temporal cortex at a preclinical stage of AD or PART (Figure 4C). By contrast, SUVRs in stage III/IV and V/VI VOIs were much less variable among HCs, and all 17 AD-spectrum (MCI + AD) cases exhibited increased SUVRs beyond the HC range in either of these VOIs (Figure 4C). Moreover, the radioligand accumulation in stage V/VI VOI (Figure 4C) was significantly correlated with the severity of dementia as assessed by clinical dementia rating sum of boxes (CDRSoB) ($r = 0.671$; p = 0.003; Figure 4D), whereas other stage VOIs did not show significant correlations.

These results indicate that ^{18}F-PM-PBB3 could detect tau depositions at preclinical and prodromal stages in the AD spectrum and PART and that the formation of ^{18}F-PM-PBB3-positive tau fibrils is intimately associated with functional deteriorations of neocortical neurons in subjects with cognitive declines.

The utility of ^{18}F-PM-PBB3 for evaluations of four-repeat tau pathologies was also examined in 16 PSP-Richardson patients who were negative for ^{11}C-PiB-PET (mean age ± SD, 71.5 ± 6.5 years). Severities of the disease in these cases were assessed using PSP Rating Scale (PSPRS) (Golbe and Ohman-Strickland, 2007). High ^{18}F-PM-PBB3 retention was observed in the subthalamic nucleus and midbrain of PSP patients relative to HCs, was progressively intensified within these subcortical structures, and was expanded to the neocortical area, including the gray and white matter of the primary motor cortex together with increases in PSPRS scores (Figure 5A). Voxelwise PET and magnetic resonance imaging (MRI) assays revealed high spatial accordance of the radioligand accumulation and brain atrophy in the subthalamic nucleus and midbrain as compared to HCs (Figure 5B). VOI-based analyses also showed significant elevations of radioligand SUVRs in the subcortical areas of PSP patients compared to HCs (Figure 5C). In particular, SUVR in the subthalamic nucleus (Williams et al., 2007) was increased in all PSP cases with little overlap with HC values (Figure 5C) and was closely, significantly, correlated with PSPRS scores (Figure 5D; r = 0.566; p = 0.018). There were no gender differences between HCs and MCI/AD or PSP patients.

Intraindividual Links between ^{18}F-PM-PBB3 PET Data and Tau Pathologies in Biopsy and Autopsy Brain Tissues Proven in CBD, PSP, and PiD Patients

We obtained histopathological evidence that *in vivo* ^{18}F-PM-PBB3 binding reflects the abundance of three- and four-repeat tau inclusions in patients with biopsy- and autopsy-confirmed FTLD tauopathies. A clinical phenotype case of corticobasal syndrome (CBS) underwent a brain biopsy as reported by Arakawa et al. (2020); Figure S8A. Neuropathological and biochemical examinations of the biopsy sample from the middle frontal gyrus revealed the presence of four-repeat tau aggregates, which are characteristic of CBD (Arakawa et al., 2020; Figure 6A). Subsequent PET scans of this case showed negativity for ^{11}C-PiB and notable increases of ^{18}F-PM-PBB3 retentions in the primary motor cortex, basal ganglia, and brainstem consistent with the regional localization of CBD tau pathologies (Kouri et al., 2011) and middle frontal gyrus (Figures 6A and S8A).

Brain autopsy was also performed for a PSP-Richardson patient who had received an ^{18}F-PM-PBB3 PET scan (see Supplemental Information for clinical information), and a definitive diagnosis of PSP (Cairns et al., 2007) was made on the basis of neuropathological observations. *In vivo* ^{18}F-PM-PBB3 radiosignals in the brain parenchyma were primarily concentrated in the subthalamic nucleus and midbrain (Figures 3A and 5A [asterisked images] and 6B and 7 [top row]). Histochemical and immunohistochemical analyses of the autopsied specimen identified a high abundance of GB- and AT8-stained tufted astrocytes in the tegmentum and substantia nigra of the midbrain and subthalamic nucleus, and these tau inclusions were fluorescently labeled with nonradioactive PM-PBB3 (Figures 6B and S8B).

Moreover, we conducted brain autopsy of a patient with the clinical diagnosis of behavioral variant frontotemporal dementia (bvFTD), who had undergone an ^{18}F-PM-PBB3 PET scan (see Supplemental Information for clinical information). Neuropathological examinations of the autopsied tissues provided a definitive diagnosis of PiD (Cairns et al., 2007). Increased retentions of ^{18}F-PM-PBB3 were noticeable in frontal and temporal cortices, but not in the occipital cortex (Figure 6C). Histopathological assays showed numerous intraneuronal Pick bodies along with neuropil threads doubly labeled with AT8 and PM-PBB3 fluorescence in the inferior frontal gyrus, in contrast to noticeable pathologies in the primary visual cortex (Figure 6C). Taken together, these data on the imaging-pathology relationships within a subject strongly support the capability of ^{18}F-PM-PBB3 for high-contrast visualization of three- and four-repeat tau deposits in the FTLD spectrum.

Individual-Based Assessments of Tau Pathologies in Living Patients with Diverse FTLD Phenotypes

To test the feasibility of ^{18}F-PM-PBB3 for evaluations of FTLD tau pathologies on an individual basis, patients with diverse clinical FTLD phenotypes were scanned with this radioligand (Figure 7). The absence of overt AD pathologies was confirmed by the negativity for ^{11}C-PiB-PET in all these cases. As compared to a case included in the above-mentioned PSP-Richardson group (top row in Figure 7), a patient with PSP parkinsonism (PSP-P), which is clinically characterized by mild motor disability compared to PSP-Richardson, showed a modestly increased tracer uptake confined to the subthalamic nucleus (second row in Figure 7). A patient clinically diagnosed as non-AD CBS showed high radioligand binding in the primary motor cortex, including below white matter and subcortical regions, such as the subthalamic nucleus, globus pallidus, and midbrain, with left-right asymmetry, which was predominant on the side contralateral to the more affected body side (third row in Figure 7). These changes indicate the existence of CBD tau pathologies underlying the symptomatic manifestation of CBS. Similarly, left-side-dominant enhancements of radioligand retention were observed in gray and white matter of the primary motor cortex (i.e., precentral gyrus) and subcortical structures of a patient with progressive non-fluent aphasia (PNFA) (fourth row in Figure 7). It is thus likely that the verbal symptoms of this individual represented by anarthria were chiefly attributable to CBD tau pathologies involving an inferior portion of the left precentral gyrus. Furthermore, a patient with bvFTD presented elevations of ^{18}F-PM-PBB3 uptake in the lateral superior frontal gyrus and prefrontal cortex with little involvement of the primary motor cortex and subcortical structures (bottom row in Figure 7). Taken together, the tracer topographies matched the neuroanatomical variabilities of the FTLD spectrum, indicating that ^{18}F-PM-PBB3 could provide an accurate diagnosis based on the evaluation of pathological backgrounds on an individual basis.

In light of the current PET observations, we constructed a schematic map illustrating that the topology of ^{18}F-PM-PBB3 radiosignals is indicative of PSP, CBD, and PiD pathologies as the bases of five different clinical phenotypes of FTLD (Figure 8; clinicopathological relationships were modified from Williams and Lees, 2009). The subcortical dominance of tau depositions
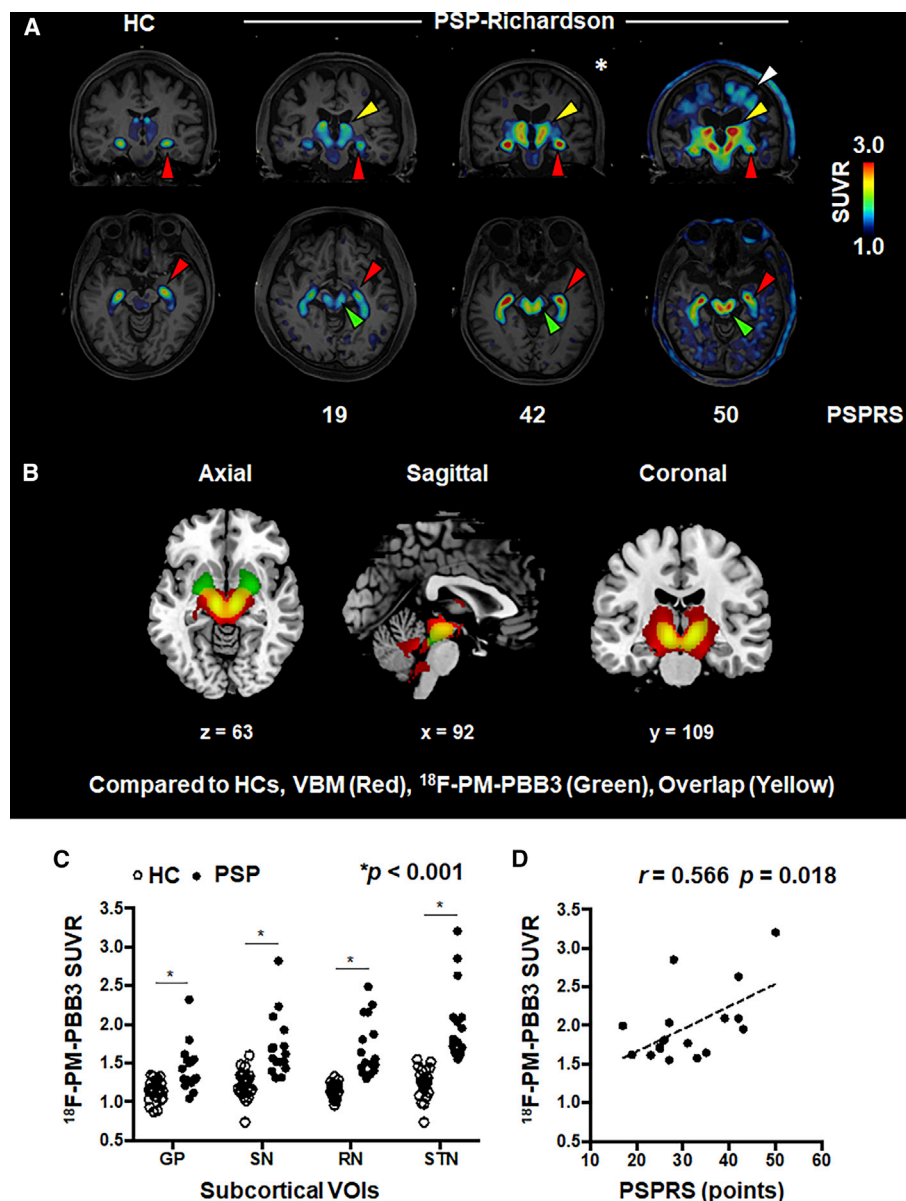
Figure 5. Associations between Clinical Disease Severity and the Extension of ¹⁸F-PM-PBB3 Binding in PSP-Richardson Patients

(A) Coronal (upper) and axial (lower) ¹⁸F-PM-PBB3-PET images of HC and PSP-Richardson patients with different disease severities scored by PSPRS. The red arrowheads point to the choroid plexus. PSP patients showed intensification of ¹⁸F-PM-PBB3 binding in the subthalamic nucleus and neighboring thalamic and basal ganglia areas (yellow arrowhead) and midbrain (green arrowhead) and expansion to the primary motor and adjacent cerebral cortices containing white matter (white arrowhead) along with the clinical advancement. The asterisked image was derived from an autopsy-confirmed PSP case.

(B) Voxel-based analyses of brain atrophy (voxel-based morphometry [VBM]; red), ¹⁸F-PM-PBB3 signal increase (green), and their spatial overlaps (yellow) in PSP-Richardson patients relative to HCs ($p < 0.05$, familywise error corrected at cluster level). Statistical maps are displayed in the Montreal Neurological Institute coordinate space.

(C) Comparisons of ¹⁸F-PM-PBB3 uptake in subcortical VOIs, including the globus pallidus (GP), substantia nigra (SN), raphe nucleus (RN), and subthalamic nucleus (STN) between 23 HCs (white circles) and 16 PSP-Richardson patients (black circles). *$p < 0.001$ by two-sample t test.

(D) Correlation of ¹⁸F-PM-PBB3 SUVR values in the STN with PSPRS points. $r = 0.566$ and $p = 0.018$ by Pearson's correlation analysis.

characterizes pathological changes in PSP, whereas a spatial expansion of areas with ¹⁸F-PM-PBB3-positive tau lesions to neocortical gray and white matter centralized at the primary motor cortex may occur with disease progression. More widespread and intense accumulations in the neocortex, often with left-right asymmetry, could suggest the presence of CBD pathologies provoking clinical manifestations of CBS and PNFA. CBD tau abnormalities may also give rise to bvFTD phenotypes, but enhanced PET
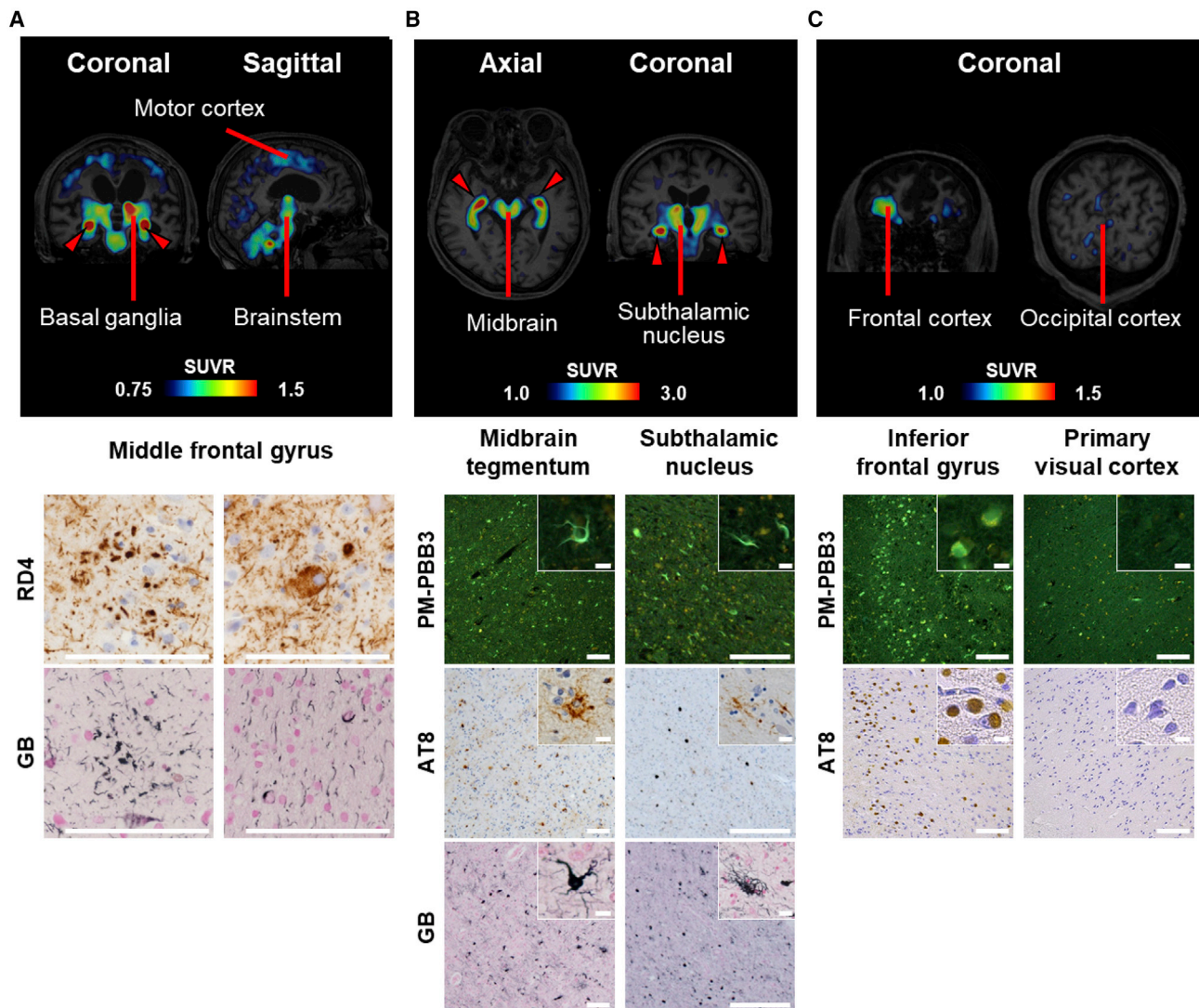
Figure 6. PET Images of ^{18}F-PM-PBB3 Retentions in Patients with Biopsy-Confirmed CBD and Autopsy-Confirmed PSP and PiD

(A) Coronal and sagittal brain images of a 68-year-old subject clinically diagnosed with CBS (upper panels). Enhanced radioligand binding was observed in the primary motor and adjacent cortices and subcortical regions, including basal ganglia, subthalamic nucleus, midbrain, pons, and choroid plexus (red arrowheads). Neuropathological assays of biopsy tissues collected from the middle frontal gyrus revealed the existence of astrocytic plaques, ballooned neurons, and coiled bodies stained with RD4 and/or GB in the cortex and corticomedullary junction (lower panels), in agreement with CBD tau pathologies.

(B) Axial and coronal ^{18}F-PM-PBB3 PET images of a 65-year-old patient with a clinical diagnosis of PSP-Richardson (PSP-3, upper panels). The radioligand binding was augmented in the midbrain, subthalamic nucleus, neighboring subcortical structures, and choroid plexus (red arrowheads). Brain autopsy conducted 2 years after the PET scan demonstrated abundant accumulation of tufted astrocytes stained with non-radiolabeled PM-PBB3, AT8, and GB in the midbrain tegmentum and subthalamic nucleus (lower panels), indicating PSP as a definite diagnosis of this individual.

(C) Coronal ^{18}F-PM-PBB3 PET images of a 59-year-old patient clinically diagnosed with bvFTD (PiD-2, upper panels). Accumulations of radiosignals were noticeable in the frontal cortex, in contrast with a lack of radioligand binding in the occipital cortex. Brain autopsy was carried out 1 year after the PET scan, showing great abundance of Pick bodies and neuropil threads stained with non-radiolabeled PM-PBB3 and AT8 in the inferior frontal gyrus (lower panels). This was in sharp distinction from the few tau pathologies in the primary visual cortex (lower panels), collectively supporting a definite diagnosis of this case as PiD. Scale bars, 10 μm (inset) and 100 μm.

signals in the frontal and temporal cortices with fewer involvements of the primary motor cortex and subcortical regions imply bvFTD due to PiD pathologies. Hence, PET imaging with ^{18}F-PM-PBB3 potentially offers identification of the tau neuropathology linked to the clinical features of FTLD in each individual case.

DISCUSSION

Diagnostic evaluations of neurodegenerative tauopathies have been impeded by the lack of one-to-one associations between diverse neuropathological and clinical phenotypes. PET imaging with our novel radioligand, ^{18}F-PM-PBB3, has been proven to
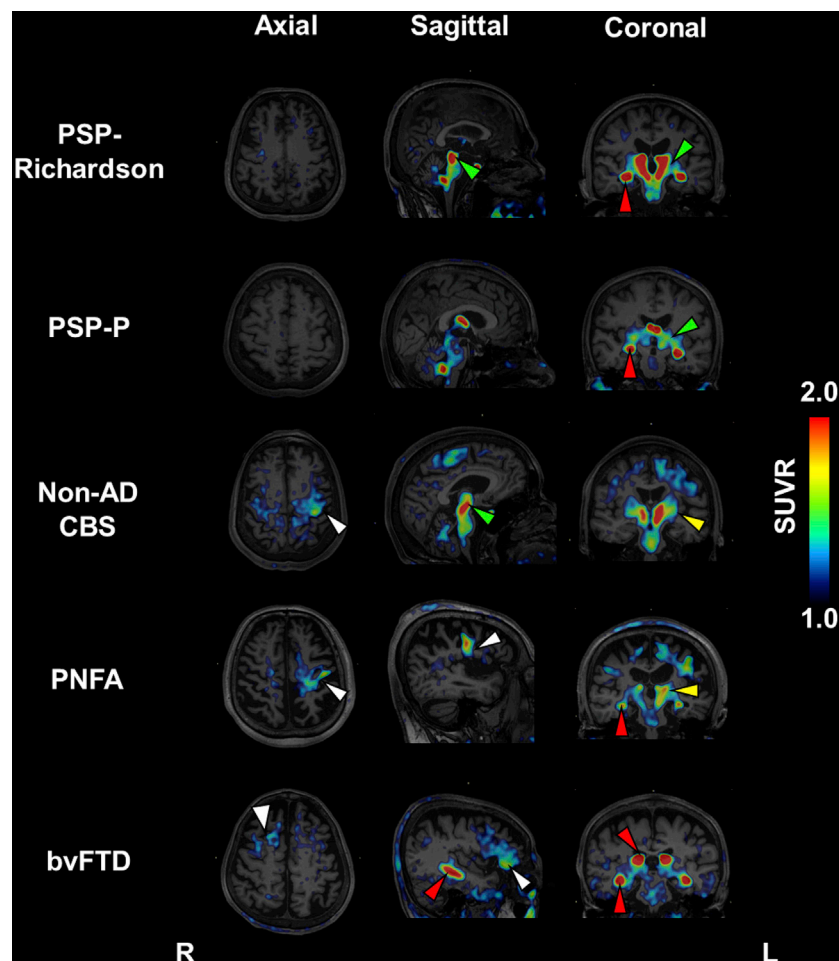
Figure 7. The Topology of *In Vivo* ^{18}F-PM-PBB3 Binding in Patients with Diverse Clinical Subtypes of FTLD

Areas with intensified radiosignals, including the primary motor and cortices (white arrowheads), basal ganglia (yellow arrowheads), subthalamic nucleus/midbrain (green arrowheads), and choroid plexus (red arrowheads), are indicated in orthogonal ^{18}F-PM-PBB3 PET images of individual patients. From top to bottom: a 65-year-old male clinically diagnosed with PSP-Richardson and a PSPRS score of 42 points and also autopsy-confirmed PSP; a 62-year-old female clinically diagnosed with PSP-P and a PSPRS score of 20 points; a 65-year-old female clinically diagnosed with non-AD CBS and a Mini Mental State Examination (MMSE) score of 27 points; a 75-year-old male clinically diagnosed with PNFA and an MMSE score of 30 points; and a 72-year-old female clinically diagnosed with bvFTD and an MMSE score of 11 points.

capture a wide range of tau fibrils with different isoform compositions, conformations, and ultrastructural dimensions with contrast and dynamic range adequate for individual-based assessments of AD- and FLTD-spectrum syndromes. Of note is that imaging-neuropathology relationships within single subjects undergoing biopsy or autopsy provided compelling evidence for the ability of the present PET technology to detect tau deposits in CBD, PSP, and PiD. In addition, sensitive detection of tau inclusions in a tauopathy model mouse was enabled with a cellular scale by intravital two-photon laser microscopy and non-labeled PM-PBB3 and with a regional scale by PET and ^{18}F-PM-PBB3. This multi-scale imaging system could prove useful for non-clinical investigations of neuropathologies, which can be combined with functional analyses exemplified by microscopic calcium assays and macroscopic functional MRI to clarify links between tau accumulations and neuronal dysfunctions from single-cell to brain-wide levels.

PBB derivatives exhibit unique features represented by high reactivity with three-repeat or four-repeat tau assemblies in FTLD patients and mouse models (Maruyama et al., 2013; Ono et al., 2017), in contrast to weak *in vitro* and *in vivo* labeling of these aggregates with flortaucipir and its second-generation analogs (Aguero et al., 2019; Hostetler et al., 2016; Leuzy et al., 2020; Ono et al., 2017; Schonhaut et al., 2017). One of the flor-

taucipir derivatives, ^{18}F-PI-2620, was reported to react with four- and three-repeat tau inclusions in FTLD brains (Brendel et al., 2020; Kroth et al., 2019), but its capability to sensitively visualize FTLD-spectrum tau pathologies has been controversial because of a lack of compelling evidence for the agreement of radioligand retentions with PSP, CBD, and PiD tau topologies. A latest clinical PET study has demonstrated that DVR for ^{18}F-PI-2620 in the globus pallidus provided the largest difference between PSP-Richardson and control groups by approximately 20% and that the sensitivity and specificity of this separation were 85% and 77%, respectively (Brendel et al., 2020). In the present work, the difference in SUVR for ^{18}F-PM-PBB3 in the subthalamic nucleus between the PSP (PSP-Richardson and non-Richardson) and control groups was 56% (1.93 versus 1.24; Table S3), and the sensitivity and specificity for the group separation determined by a receiver operating characteristic curve analysis were 94% and 96%, respectively (Figures S9A and S9B). Furthermore, SUVRs for ^{18}F-PM-PBB3 in the subthalamic nucleus were intimately correlated with PSPRS, in contrast to the lack of correlations between ^{18}F-PI-2620 DVRs and clinical severity (Brendel et al., 2020). Notwithstanding that head-to-head comparisons of these three radioligands in the same FTLD-tau cases will be required for unbiased evaluations of their capabilities, it is conceivable that ^{18}F-PM-PBB3 has the most promising ability to detect FTLD tau deposits among currently available radioprobes in view of the previous and current reports.

Owing to the *in vivo* stability against metabolic conversions, ^{18}F-PM-PBB3 produced a higher signal-to-noise ratio than ^{11}C-PBB3 for detection of tau pathologies. This benefit could lead to a higher signal-to-noise ratio produced by ^{18}F-PM-PBB3 than ^{11}C-PBB3 for detection tau pathologies. Moreover, higher BP values of ^{18}F-PM-PBB3 were shown in homogenates of rTg4510 mouse and PSP brain tissues. According to the low
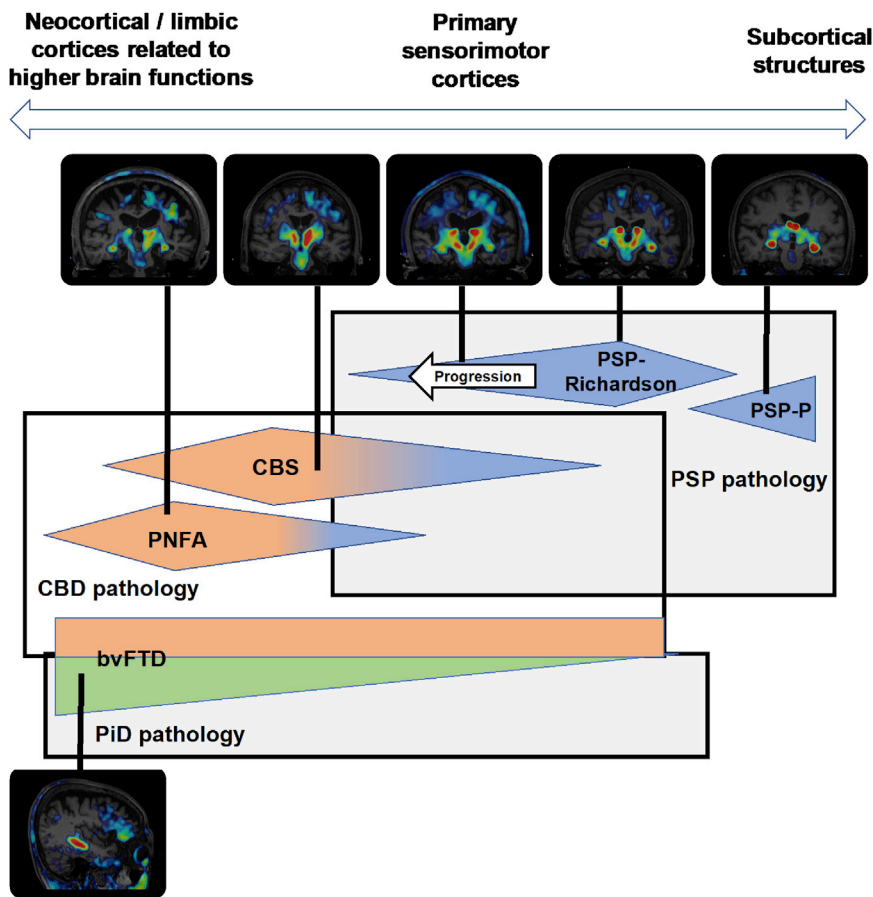
Figure 8. A Schematic Presentation of PET-Detectable Tau Topologies in Association with Clinical and Neuropathological Nosologies of FTLD Syndromes

Three tau neuropathologies underlie five clinical phenotypes, and the neocortex-to-subcortex gradient of tau depositions varies as a function of clinicopathological entity and progression of the disease. Patients whose symptomatic manifestations are confined to parkinsonism are likely to exhibit ^{18}F-PM-PBB3 binding localized to subcortical areas (rightward), although patients with cortical symptoms, such as apraxia and aphasia, may frequently display the radioligand binding primarily in the frontotemporal cortex (leftward).

The current data also provide evidence for the *in vivo* performance of ^{18}F-PM-PBB3 as a diagnostic adjunct to the identification and differentiation of various clinical FTLD subtypes on a neuropathological basis. Indeed, distinctions between AD/PART and CBD/PSP in PNFA and CBS and among AD/PART, CBD/PSP, and PiD in bvFTD were allowed for each case according to the topology of PM-PBB3-positive tau deposits. Because such clear separations have not been possible with the use of previous tau PET ligands (Endo et al., 2019; Schonhaut et al., 2017) and other imaging modalities, such as volumetric MRI, the current technology paves the way for the construction of a biomonitoring system for the selection of an adequate disease-modifying therapeutic.

Toward the eventual goal of establishing a PET-based system for the early diagnosis and differentiation of diverse neurodegenerative dementias with ^{18}F-PM-PBB3, further longitudinal and clinicopathological assessments will be required. It will be of particular significance that a reliable protocol for the image acquisition and analysis is secured by a longitudinal cohort study with a larger scale. Moreover, careful and thorough investigations of ^{18}F-PM-PBB3-PET data in subjects with autopsy-confirmed neuropathologies will allow evaluations of the present imaging technology for the differentiation of FTLD syndromes and related atypical dementias with and without parkinsonism. Our preliminary findings imply the negativity for a PET scan with ^{18}F-PM-PBB3-PET in a typical amyotrophic lateral sclerosis (ALS) case with upper motor impairments and a case with idiopathic Parkinson's disease (Figure S9C), but the specificity of the imaging probe will need to be extensively pursued in a sufficient number of patients with *post mortem* data.

Along with technical benefits, several issues should also be considered regarding the utilization of ^{18}F-PM-PBB3 in clinical PET scans. The accumulation of radioactivity in the choroid plexus might hinder quantitative assessments of tau depositions in neighboring structures, including the hippocampus, although

B_{max} of these samples relative to AD brain tissues and a previous biochemical finding (Narasimhan et al., 2017), we postulate that the packaging density of tau fibrils in mouse models and PSP is lower than that of AD. It is accordingly likely that ^{18}F-PM-PBB3 is capable of capturing less mature tau assemblies at an earlier stage than ^{11}C-PBB3, providing an explanation for the markedly greater specific binding of ^{18}F-PM-PBB3 than ^{11}C-PBB3 in PET scans of rTg4510 mouse and PSP brains. This notion was further supported by supplementary PET and *ex vivo* autoradiographic observations in another tauopathy model, PS19 (Yoshiyama et al., 2007), that less mature tau assemblies in the hippocampus of this strain were sensitively captured by ^{18}F-PM-PBB3 (Figure S10), in contrast to the unsuccessful visualization of these lesions by ^{11}C-PBB3 (Maruyama et al., 2013).

Similar to previous indications of prion-like tau dissemination in AD brains capturable by PET with other probes (Betthauser et al., 2020; Cho et al., 2016; Jack et al., 2018; Leuzy et al., 2020; Pascoal et al., 2018; Shimada et al., 2016), ^{18}F-PM-PBB3 was capable of visualizing the spatial spread of tau depositions in line with Braak's tau staging, with regional radioligand retentions correlated with clinical advancements assessed by CDRSoB. Significantly, enhanced radiosignals in the subthalamic nucleus were concurrent with the symptomatic advancement of PSP scored by PSPRS and were expanded from subcortical to neocortical areas, seemingly in accordance with emergences of cognitive deficits.

this did not overtly influence the measurement of radioligand retentions in the parahippocampal gyrus, which is the area involved in tau pathologies at the earliest Braak stage. As implied in a PSP case (Table S2), increased retention of ^{18}F-PM-PBB3 might occur in the cerebellar cortex, which possibly reflects tau deposits in this area, leading to underestimation of SUVR in a target tissue. Although the present work consistently employs the cerebellar reference across various disorders, the use of extracted reference voxels would circumvent this technical issue (Endo et al., 2019; Kimura et al., 2016; Takahata et al., 2019). Another caveat might be the photoisomerization of PM-PBB3, which is similar to the reported property of PBB3 (Hashimoto et al., 2014). Our data indicated that the conversion of PBB3 and PM-PBB3 to their isomers could be entirely blocked using a UV-free light-emitting diode (LED) light in the radiosynthesis and administration to subjects, requiring small additional equipment in nuclear medicine facilities.

The translational research workflow with PM-PBB3 offers a seamless evaluation of candidate anti-tau therapeutics (Congdon and Sigurdsson, 2018; Shoeibi et al., 2018) in non-clinical and subsequent clinical settings. Comparisons between efficacies of such potential drugs in animal models and humans with the same imaging-based biomarker will also help refine these models in view of their resemblance to tauopathy cases.

To our conclusion, the new bimodal imaging agent, PM-PBB3, enabled high-contrast optical and PET detection of diverse tau conformers at cellular, regional, and global scales in animal brains. This probe also captured AD- and FTLD-type tau pathologies with a dynamic range sufficient for differentiation and staging of tauopathy subtypes in each subject, reinforcing investigations of the neuropathological basis of clinical phenotypes in living tauopathy cases.

STAR★METHODS

Detailed methods are provided in the online version of this paper and include the following:

- KEY RESOURCES TABLE
- RESOURCE AVAILABILITY
  - Lead Contact
  - Materials Availability
  - Data and Code Availability
- EXPERIMENTAL MODEL AND SUBJECT DETAILS
  - Mice
  - Human subjects
  - Clinical histories of autopsied patients
  - Clinical histories of patients with diverse FTLD spectrum and non-tauopathies
- METHOD DETAILS
  - Compounds and Antibodies
  - Molecular Dynamics and MM/GBSA calculations
  - Radiosynthesis
  - Stability of ^{18}F-PM-PBB3 and ^{11}C-PBB3 under UV-cut condition
  - Postmortem brain tissues
  - Neuropathologic assessment
  - *In vitro* binding assay

- *In vitro* and *ex vivo* autoradiography
  - Histological examination
  - *In vivo* two-photon fluorescence microscopy
  - *In vivo* PET imaging in mice
  - Radiometabolite analysis in mice
  - Tissue extraction and immunoblot analyses
  - *In vivo* MRI and PET Imaging in Human Subjects
  - Radiometabolite analysis in human subjects
  - Image analyses in Human Subjects
  - Assessing Tau Deposits Associated with AD
  - Assessing Tau Deposits Associated with PSP-Richardson
- QUANTIFICATION AND STATISTICAL ANALYSIS

AUTHOR CONTRIBUTIONS

Conceptualization, Y. Takado, M.-R.Z., T.S., M. Shigeta, N.S., M.H., and H. Shimada; Investigation, K. Tagai, M. Ono, S.K., K. Takahata, M.K., H. Shinotoh, Y. Sano, Y. Yamamoto, K.M., C.S., Y.K., M.I., H.T., M.S., and M.T.; Resources, K.K., T.K., M. Okada, H.A., H. Suzuki, M. Onaya, T.T., K.A., N. Arai, N. Araki, Y. Saito, J.Q.T., V.M.-Y.L., S.K.M., Y. Yamaguchi, and Y. Tomita; Writing – Original Draft, K. Tagai and M. Ono; Writing – Review & Editing, K. Tagai, M. Ono, Y. Takado, and M.H.; Supervision, Y. Takado and M.H.; Project Administration, N.S. and H. Shimada; Funding Acquisition, N.S., M.H., and H. Shimada.

REFERENCES

Aguero, C., Dhaynaut, M., Normandin, M.D., Amaral, A.C., Guehl, N.J., Neelamegam, R., Marquie, M., Johnson, K.A., El Fakhri, G., Frosch, M.P., and Gomez-Isla, T. (2019). Autoradiography validation of novel tau PET tracer [F-18]-MK-6240 on human postmortem brain tissue. Acta Neuropathol. Commun. 7, 37.

Akaike, H. (1973). Information theory and an extension of the maximum likelihood principle. In 2nd International Symposium on Information Theory, B.N. Petrov and F. Csaki, eds. (Akadémiai Kiadó), pp. 267–281.

Arakawa, A., Saito, Y., Seki, T., Mitsutake, A., Sato, T., Katsumata, J., Maekawa, R., Hideyama, T., Tamura, K., Hasegawa, M., and Shiio, Y. (2020). Corticobasal degeneration with deep white matter lesion diagnosed by brain biopsy. Neuropathology 40, 287–294.

Armstrong, M.J., Litvan, I., Lang, A.E., Bak, T.H., Bhatia, K.P., Borroni, B., Boxer, A.L., Dickson, D.W., Grossman, M., Hallett, M., et al. (2013). Criteria for the diagnosis of corticobasal degeneration. Neurology 80, 496–503.

Betthauser, T.J., Koscik, R.L., Jonaitis, E.M., Allison, S.L., Cody, K.A., Erickson, C.M., Rowley, H.A., Stone, C.K., Mueller, K.D., Clark, L.R., et al. (2020). Amyloid and tau imaging biomarkers explain cognitive decline from late middle-age. Brain 143, 320–335.

Boluda, S., Toledo, J.B., Irwin, D.J., Raible, K.M., Byrne, M.D., Lee, E.B., Lee, V.M., and Trojanowski, J.Q. (2014). A comparison of Aβ amyloid pathology staging systems and correlation with clinical diagnosis. Acta Neuropathol. 128, 543–550.

Braak, H., and Braak, E. (1991). Neuropathological staging of Alzheimer-related changes. Acta Neuropathol. 82, 239–259.

Brendel, M., Schönecker, S., Höglinger, G., Lindner, S., Havla, J., Blautzik, J., Sauerbeck, J., Rohrer, G., Zach, C., Vettermann, F., et al. (2018). [18F]-THK5351 PET correlates with topology and symptom severity in progressive supranuclear palsy. Front. Aging Neurosci. 9, 440.

Brendel, M., Barthel, H., van Eimeren, T., Marek, K., Beyer, L., Song, M., Palleis, C., Gehmeyr, M., Fietzek, U., Respondek, G., et al. (2020). Assessment of ^{18}F-PI-2620 as a biomarker in progressive supranuclear palsy. JAMA Neurol. e202526.

Buée, L., Bussière, T., Buée-Scherrer, V., Delacourte, A., and Hof, P.R. (2000). Tau protein isoforms, phosphorylation and role in neurodegenerative disorders. Brain Res. Brain Res. Rev. 33, 95–130.

Cairns, N.J., Bigio, E.H., Mackenzie, I.R., Neumann, M., Lee, V.M., Hatanpaa, K.J., White, C.L., 3rd, Schneider, J.A., Grinberg, L.T., Halliday, G., et al.; Consortium for Frontotemporal Lobar Degeneration (2007). Neuropathologic diagnostic and nosologic criteria for frontotemporal lobar degeneration: consensus of the Consortium for Frontotemporal Lobar Degeneration. Acta Neuropathol. 114, 5–22.

Chien, D.T., Szardenings, A.K., Bahri, S., Walsh, J.C., Mu, F., Xia, C., Shankle, W.R., Lerner, A.J., Su, M.Y., Elizarov, A., and Kolb, H.C. (2014). Early clinical PET imaging results with the novel PHF-tau radioligand [F18]-T808. J. Alzheimers Dis. 38, 171–184.

Cho, H., Choi, J.Y., Hwang, M.S., Kim, Y.J., Lee, H.M., Lee, H.S., Lee, J.H., Ryu, Y.H., Lee, M.S., and Lyoo, C.H. (2016). In vivo cortical spreading pattern of tau and amyloid in the Alzheimer disease spectrum. Ann. Neurol. 80, 247–258.

Congdon, E.E., and Sigurdsson, E.M. (2018). Tau-targeting therapies for Alzheimer disease. Nat. Rev. Neurol. 14, 399–415.

Endo, H., Shimada, H., Sahara, N., Ono, M., Koga, S., Kitamura, S., Niwa, F., Hirano, S., Kimura, Y., Ichise, M., et al. (2019). In vivo binding of a tau imaging probe, [^{11}C]PBB3, in patients with progressive supranuclear palsy. Mov. Disord. 34, 744–754.

Falcon, B., Zhang, W., Murzin, A.G., Murshudov, G., Garringer, H.J., Vidal, R., Crowther, R.A., Ghetti, B., Scheres, S.H.W., and Goedert, M. (2018). Structures of filaments from Pick's disease reveal a novel tau protein fold. Nature 561, 137–140.

Forrest, S.L., Kril, J.J., and Halliday, G.M. (2019). Cellular and regional vulnerability in frontotemporal tauopathies. Acta Neuropathol. 138, 705–727.

Frisch, M.J.T., G.W., Schlegel, H.B., Scuseria, G.E., Robb, M.A., Cheeseman, J.R., Scalmani, G., Barone, V., Petersson, G.A., Nakatsuji, H., et al. (2016). Gaussian 16, Revision B.01 (Wallingford CT: Gaussian, Inc.).

Golbe, L.I., and Ohman-Strickland, P.A. (2007). A clinical rating scale for progressive supranuclear palsy. Brain 130, 1552–1565.

Gorno-Tempini, M.L., Hillis, A.E., Weintraub, S., Kertesz, A., Mendez, M., Cappa, S.F., Ogar, J.M., Rohrer, J.D., Black, S., Boeve, B.F., et al. (2011). Classification of primary progressive aphasia and its variants. Neurology 76, 1006–1014.

Harada, R., Okamura, N., Furumoto, S., Furukawa, K., Ishiki, A., Tomita, N., Tago, T., Hiraoka, K., Watanuki, S., Shidahara, M., et al. (2016). 18F-THK5351: a novel PET radiotracer for imaging neurofibrillary pathology in Alzheimer disease. J. Nucl. Med. 57, 208–214.

Harada, R., Ishiki, A., Kai, H., Sato, N., Furukawa, K., Furumoto, S., Tago, T., Tomita, N., Watanuki, S., Hiraoka, K., et al. (2018). Correlations of ^{18}F-THK5351 PET with postmortem burden of tau and astrogliosis in Alzheimer disease. J. Nucl. Med. 59, 671–674.

Hashimoto, H., Kawamura, K., Igarashi, N., Takei, M., Fujishiro, T., Aihara, Y., Shiomi, S., Muto, M., Ito, T., Furutsuka, K., et al. (2014). Radiosynthesis, photo-isomerization, biodistribution, and metabolite analysis of 11C-PBB3 as a clinically useful PET probe for imaging of tau pathology. J. Nucl. Med. 55, 1532–1538.

Hashimoto, H., Kawamura, K., Takei, M., Igarashi, N., Fujishiro, T., Shiomi, S., Watanabe, R., Muto, M., Furutsuka, K., Ito, T., et al. (2015). Identification of a major radiometabolite of [11C]PBB3. Nucl. Med. Biol. 42, 905–910.

Hauw, J.J., Daniel, S.E., Dickson, D., Horoupian, D.S., Jellinger, K., Lantos, P.L., McKee, A., Tabaton, M., and Litvan, I. (1994). Preliminary NINDS neuro-pathologic criteria for Steele-Richardson-Olszewski syndrome (progressive supranuclear palsy). Neurology 44, 2015–2019.

Höglinger, G.U., Respondek, G., Stamelou, M., Kurz, C., Josephs, K.A., Lang, A.E., Mollenhauer, B., Müller, U., Nilsson, C., Whitwell, J.L., et al.; Movement Disorder Society-endorsed PSP Study Group (2017). Clinical diagnosis of progressive supranuclear palsy: the movement disorder society criteria. Mov. Disord. 32, 853–864.

Honer, M., Gobbi, L., Knust, H., Kuwabara, H., Muri, D., Koerner, M., Valentine, H., Dannals, R.F., Wong, D.F., and Borroni, E. (2018). Preclinical evaluation of ^{18}F-RO6958948, ^{11}C-RO6931643, and ^{11}C-RO6924963 as novel PET radio-tracers for imaging tau aggregates in Alzheimer disease. J. Nucl. Med. 59, 675–681.

Hostetler, E.D., Walji, A.M., Zeng, Z., Miller, P., Bennacef, I., Salinas, C., Connolly, B., Gantert, L., Haley, H., Holahan, M., et al. (2016). Preclinical characterization of 18F-MK-6240, a promising PET tracer for in vivo quantification of human neurofibrillary tangles. J. Nucl. Med. 57, 1599–1606.

Ichise, M., Toyama, H., Innis, R.B., and Carson, R.E. (2002). Strategies to improve neuroreceptor parameter estimation by linear regression analysis. J. Cereb. Blood Flow Metab. 22, 1271–1281.

Ikonomovic, M.D., Abrahamson, E.E., Price, J.C., Mathis, C.A., and Klunk, W.E. (2016). [F-18]AV-1451 positron emission tomography retention in choroid plexus: More than "off-target" binding. Ann. Neurol. 80, 307–308.

Iqbal, K., Liu, F., and Gong, C.X. (2016). Tau and neurodegenerative disease: the story so far. Nat. Rev. Neurol. 12, 15–27.

Ishikawa, A., Tokunaga, M., Maeda, J., Minamihisamatsu, T., Shimojo, M., Takuwa, H., Ono, M., Ni, R., Hirano, S., Kuwabara, S., et al. (2018). In vivo visualization of tau accumulation, microglial activation, and brain atrophy in a mouse model of tauopathy rTg4510. J. Alzheimers Dis. 61, 1037–1052.

Jack, C.R., Jr., Wiste, H.J., Schwarz, C.G., Lowe, V.J., Senjem, M.L., Vemuri, P., Weigand, S.D., Therneau, T.M., Knopman, D.S., Gunter, J.L., et al. (2018). Longitudinal tau PET in ageing and Alzheimer's disease. Brain 141, 1517–1528.

Kanazawa, M., Shimohata, T., Toyoshima, Y., Tada, M., Kakita, A., Morita, T., Ozawa, T., Takahashi, H., and Nishizawa, M. (2009). Cerebellar involvement in

progressive supranuclear palsy: A clinicopathological study. Mov. Disord. *24*, 1312–1318.

Kikuchi, A., Okamura, N., Hasegawa, T., Harada, R., Watanuki, S., Funaki, Y., Hiraoka, K., Baba, T., Sugeno, N., Oshima, R., et al. (2016). In vivo visualization of tau deposits in corticobasal syndrome by 18F-THK5351 PET. Neurology *87*, 2309–2316.

Kimura, Y., Ichise, M., Ito, H., Shimada, H., Ikoma, Y., Seki, C., Takano, H., Kitamura, S., Shinotoh, H., Kawamura, K., et al. (2015). PET quantification of tau pathology in human brain with 11C-PBB3. J. Nucl. Med. *56*, 1359–1365.

Kimura, Y., Endo, H., Ichise, M., Shimada, H., Seki, C., Ikoma, Y., Shinotoh, H., Yamada, M., Higuchi, M., Zhang, M.R., and Suhara, T. (2016). A new method to quantify tau pathologies with (11)C-PBB3 PET using reference tissue voxels extracted from brain cortical gray matter. EJNMMI Res. *6*, 24.

Klein, A., and Tourville, J. (2012). 101 labeled brain images and a consistent human cortical labeling protocol. Front. Neurosci. *6*, 171.

Klunk, W.E., Wang, Y., Huang, G.F., Debnath, M.L., Holt, D.P., and Mathis, C.A. (2001). Uncharged thioflavin-T derivatives bind to amyloid-beta protein with high affinity and readily enter the brain. Life Sci. *69*, 1471–1484.

Koga, S., Josephs, K.A., Ogaki, K., Labbé, C., Uitti, R.J., Graff-Radford, N., van Gerpen, J.A., Cheshire, W.P., Aoki, N., Rademakers, R., et al. (2016). Cerebellar ataxia in progressive supranuclear palsy: An autopsy study of PSP-C. Mov. Disord. *31*, 653–662.

Kouri, N., Whitwell, J.L., Josephs, K.A., Rademakers, R., and Dickson, D.W. (2011). Corticobasal degeneration: a pathologically distinct 4R tauopathy. Nat. Rev. Neurol. *7*, 263–272.

Kroth, H., Oden, F., Molette, J., Schieferstein, H., Capotosti, F., Mueller, A., Berndt, M., Schmitt-Willich, H., Darmency, V., Gabellieri, E., et al. (2019). Discovery and preclinical characterization of [^{18}F]PI-2620, a next-generation tau PET tracer for the assessment of tau pathology in Alzheimer's disease and other tauopathies. Eur. J. Nucl. Med. Mol. Imaging *46*, 2178–2189.

Lee, V.M., Goedert, M., and Trojanowski, J.Q. (2001). Neurodegenerative tauopathies. Annu. Rev. Neurosci. *24*, 1121–1159.

Lee, C.M., Jacobs, H.I.L., Marquié, M., Becker, J.A., Andrea, N.V., Jin, D.S., Schultz, A.P., Frosch, M.P., Gómez-Isla, T., Sperling, R.A., and Johnson, K.A. (2018). 18F-flortaucipir binding in choroid plexus: related to race and hippocampus signal. J. Alzheimers Dis. *62*, 1691–1702.

Lemoine, L., Leuzy, A., Chiotis, K., Rodriguez-Vieitez, E., and Nordberg, A. (2018). Tau positron emission tomography imaging in tauopathies: the added hurdle of off-target binding. Alzheimers Dement. (Amst.) *10*, 232–236.

Leuzy, A., Smith, R., Ossenkoppele, R., Santillo, A., Borroni, E., Klein, G., Ohlsson, T., Jögi, J., Palmqvist, S., Mattsson-Carlgren, N., et al. (2020). Diagnostic performance of RO948 F 18 tau positron emission tomography in the differentiation of Alzheimer disease from other neurodegenerative disorders. JAMA Neurol. *77*, 955–965.

Lowe, V.J., Curran, G., Fang, P., Liesinger, A.M., Josephs, K.A., Parisi, J.E., Kantarci, K., Boeve, B.F., Pandey, M.K., Bruinsma, T., et al. (2016). An autoradiographic evaluation of AV-1451 Tau PET in dementia. Acta Neuropathol. Commun. *4*, 58.

Maeda, J., Zhang, M.R., Okauchi, T., Ji, B., Ono, M., Hattori, S., Kumata, K., Iwata, N., Saido, T.C., Trojanowski, J.Q., et al. (2011). In vivo positron emission tomographic imaging of glial responses to amyloid-beta and tau pathologies in mouse models of Alzheimer's disease and related disorders. J. Neurosci. *31*, 4720–4730.

Maier, J.A., Martinez, C., Kasavajhala, K., Wickstrom, L., Hauser, K.E., and Simmerling, C. (2015). ff14SB: improving the accuracy of protein side chain and backbone parameters from ff99SB. J. Chem. Theory Comput. *11*, 3696–3713.

Maruyama, M., Shimada, H., Suhara, T., Shinotoh, H., Ji, B., Maeda, J., Zhang, M.R., Trojanowski, J.Q., Lee, V.M., Ono, M., et al. (2013). Imaging of tau pathology in a tauopathy mouse model and in Alzheimer patients compared to normal controls. Neuron *79*, 1094–1108.

McKhann, G., Drachman, D., Folstein, M., Katzman, R., Price, D., and Stadlan, E.M. (1984). Clinical diagnosis of Alzheimer's disease: report of the NINCDS-ADRDA Work Group under the auspices of Department of Health and Human Services Task Force on Alzheimer's Disease. Neurology *34*, 939–944.

Mishra, S.K., and Koča, J. (2018). Assessing the performance of MM/PBSA, MM/GBSA, and QM-MM/GBSA approaches on protein/carbohydrate complexes: effect of implicit solvent models, QM methods, and entropic contributions. J. Phys. Chem. B *122*, 8113–8121.

Murugan, N.A., Nordberg, A., and Ågren, H. (2018). Different positron emission tomography tau tracers bind to multiple binding sites on the tau fibril: insight from computational modeling. ACS Chem. Neurosci. *9*, 1757–1767.

Nagae, M., Mishra, S.K., Hanashima, S., Tateno, H., and Yamaguchi, Y. (2017). Distinct roles for each N-glycan branch interacting with mannose-binding type Jacalin-related lectins Orysata and Calsepa. Glycobiology *27*, 1120–1133.

Narasimhan, S., Guo, J.L., Changolkar, L., Stieber, A., McBride, J.D., Silva, L.V., He, Z., Zhang, B., Gathagan, R.J., Trojanowski, J.Q., and Lee, V.M.Y. (2017). Pathological tau strains from human brains recapitulate the diversity of tauopathies in nontransgenic mouse brain. J. Neurosci. *37*, 11406–11423.

Ng, K.P., Pascoal, T.A., Mathotaarachchi, S., Therriault, J., Kang, M.S., Shin, M., Guiot, M.C., Guo, Q., Harada, R., Comley, R.A., et al. (2017). Monoamine oxidase B inhibitor, selegiline, reduces ^{18}F-THK5351 uptake in the human brain. Alzheimers Res. Ther. *9*, 25.

Ni, R., Ji, B., Ono, M., Sahara, N., Zhang, M.R., Aoki, I., Nordberg, A., Suhara, T., and Higuchi, M. (2018). Comparative in vitro and in vivo quantifications of pathologic tau deposits and their association with neurodegeneration in tauopathy mouse models. J. Nucl. Med. *59*, 960–966.

Okamoto, Y. (2004). Generalized-ensemble algorithms: enhanced sampling techniques for Monte Carlo and molecular dynamics simulations. J. Mol. Graph. Model. *22*, 425–439.

Ono, M., Sahara, N., Kumata, K., Ji, B., Ni, R., Koga, S., Dickson, D.W., Trojanowski, J.Q., Lee, V.M., Yoshida, M., et al. (2017). Distinct binding of PET ligands PBB3 and AV-1451 to tau fibril strains in neurodegenerative tauopathies. Brain *140*, 764–780.

Pascoal, T.A., Shin, M., Kang, M.S., Chamoun, M., Chartrand, D., Mathotaarachchi, S., Bennacef, I., Therriault, J., Ng, K.P., Hopewell, R., et al. (2018). In vivo quantification of neurofibrillary tangles with [^{18}F]MK-6240. Alzheimers Res. Ther. *10*, 74.

Petersen, R.C., Smith, G.E., Waring, S.C., Ivnik, R.J., Tangalos, E.G., and Kokmen, E. (1999). Mild cognitive impairment: clinical characterization and outcome. Arch. Neurol. *56*, 303–308.

Rabinovici, G.D., and Miller, B.L. (2010). Frontotemporal lobar degeneration: epidemiology, pathophysiology, diagnosis and management. CNS Drugs *24*, 375–398.

Rascovsky, K., Hodges, J.R., Knopman, D., Mendez, M.F., Kramer, J.H., Neuhaus, J., van Swieten, J.C., Seelaar, H., Dopper, E.G., Onyike, C.U., et al. (2011). Sensitivity of revised diagnostic criteria for the behavioural variant of frontotemporal dementia. Brain *134*, 2456–2477.

Robinson, J.L., Geser, F., Corrada, M.M., Berlau, D.J., Arnold, S.E., Lee, V.M., Kawas, C.H., and Trojanowski, J.Q. (2011). Neocortical and hippocampal amyloid-β and tau measures associate with dementia in the oldest-old. Brain *134*, 3708–3715.

Robinson, J.L., Corrada, M.M., Kovacs, G.G., Dominique, M., Caswell, C., Xie, S.X., Lee, V.M., Kawas, C.H., and Trojanowski, J.Q. (2018). Non-Alzheimer's contributions to dementia and cognitive resilience in The 90+ Study. Acta Neuropathol. *136*, 377–388.

Sahara, N., Perez, P.D., Lin, W.L., Dickson, D.W., Ren, Y., Zeng, H., Lewis, J., and Febo, M. (2014). Age-related decline in white matter integrity in a mouse model of tauopathy: an in vivo diffusion tensor magnetic resonance imaging study. Neurobiol. Aging *35*, 1364–1374.

Santacruz, K., Lewis, J., Spires, T., Paulson, J., Kotilinek, L., Ingelsson, M., Guimaraes, A., DeTure, M., Ramsden, M., McGowan, E., et al. (2005). Tau suppression in a neurodegenerative mouse model improves memory function. Science *309*, 476–481.

Schöll, M., Lockhart, S.N., Schonhaut, D.R., O'Neil, J.P., Janabi, M., Ossenkoppele, R., Baker, S.L., Vogel, J.W., Faria, J., Schwimmer, H.D.,

et al. (2016). PET imaging of tau deposition in the aging human brain. Neuron *89*, 971–982.

Schonhaut, D.R., McMillan, C.T., Spina, S., Dickerson, B.C., Siderowf, A., Devous, M.D., Sr., Tsai, R., Winer, J., Russell, D.S., Litvan, I., et al. (2017). ^{18}F-flortaucipir tau positron emission tomography distinguishes established progressive supranuclear palsy from controls and Parkinson disease: A multicenter study. Ann. Neurol. *82*, 622–634.

Shimada, H., Kitamura, S., Shinotoh, H., Endo, H., Niwa, F., Hirano, S., Kimura, Y., Zhang, M.R., Kuwabara, S., Suhara, T., and Higuchi, M. (2016). Association between Aβ and tau accumulations and their influence on clinical features in aging and Alzheimer's disease spectrum brains: A [11C]PBB3-PET study. Alzheimers Dement. (Amst.) *6*, 11–20.

Shoeibi, A., Olfati, N., and Litvan, I. (2018). Preclinical, phase I, and phase II investigational clinical trials for treatment of progressive supranuclear palsy. Expert Opin. Investig. Drugs *27*, 349–361.

Soto, C., and Pritzkow, S. (2018). Protein misfolding, aggregation, and conformational strains in neurodegenerative diseases. Nat. Neurosci. *21*, 1332–1340.

Spillantini, M.G., and Goedert, M. (2013). Tau pathology and neurodegeneration. Lancet Neurol. *12*, 609–622.

Takahata, K., Kimura, Y., Sahara, N., Koga, S., Shimada, H., Ichise, M., Saito, F., Moriguchi, S., Kitamura, S., Kubota, M., et al. (2019). PET-detectable tau pathology correlates with long-term neuropsychiatric outcomes in patients with traumatic brain injury. Brain *142*, 3265–3279.

Takeda, T., Uchihara, T., Arai, N., Mizutani, T., and Iwata, M. (2009). Progression of hippocampal degeneration in amyotrophic lateral sclerosis with or without memory impairment: distinction from Alzheimer disease. Acta Neuropathol. *117*, 35–44.

Takei, M., Kida, T., and Suzuki, K. (2001). Sensitive measurement of positron emitters eluted from HPLC. Appl. Radiat. Isot. *55*, 229–234.

Thal, D.R., Rüb, U., Orantes, M., and Braak, H. (2002). Phases of A beta-deposition in the human brain and its relevance for the development of AD. Neurology *58*, 1791–1800.

Tomita, Y., Kubis, N., Calando, Y., Tran Dinh, A., Méric, P., Seylaz, J., and Pinard, E. (2005). Long-term in vivo investigation of mouse cerebral microcirculation by fluorescence confocal microscopy in the area of focal ischemia. J. Cereb. Blood Flow Metab. *25*, 858–867.

Trott, O., and Olson, A.J. (2010). AutoDock Vina: improving the speed and accuracy of docking with a new scoring function, efficient optimization, and multithreading. J. Comput. Chem. *31*, 455–461.

Vermeiren, C., Motte, P., Viot, D., Mairet-Coello, G., Courade, J.P., Citron, M., Mercier, J., Hannestad, J., and Gillard, M. (2018). The tau positron-emission tomography tracer AV-1451 binds with similar affinities to tau fibrils and monoamine oxidases. Mov. Disord. *33*, 273–281.

Walker, L.C., and Jucker, M. (2015). Neurodegenerative diseases: expanding the prion concept. Annu. Rev. Neurosci. *38*, 87–103.

Wang, R., Lai, L., and Wang, S. (2002). Further development and validation of empirical scoring functions for structure-based binding affinity prediction. J. Comput. Aided Mol. Des. *16*, 11–26.

Wang, J., Wolf, R.M., Caldwell, J.W., Kollman, P.A., and Case, D.A. (2004). Development and testing of a general amber force field. J. Comput. Chem. *25*, 1157–1174.

Williams, D.R., and Lees, A.J. (2009). Progressive supranuclear palsy: clinicopathological concepts and diagnostic challenges. Lancet Neurol. *8*, 270–279.

Williams, D.R., Holton, J.L., Strand, C., Pittman, A., de Silva, R., Lees, A.J., and Revesz, T. (2007). Pathological tau burden and distribution distinguishes progressive supranuclear palsy-parkinsonism from Richardson's syndrome. Brain *130*, 1566–1576.

Yamane, T., Ishii, K., Sakata, M., Ikari, Y., Nishio, T., Ishii, K., Kato, T., Ito, K., and Senda, M.; J-ADNI Study Group (2017). Inter-rater variability of visual interpretation and comparison with quantitative evaluation of ^{11}C-PiB PET amyloid images of the Japanese Alzheimer's Disease Neuroimaging Initiative (J-ADNI) multicenter study. Eur. J. Nucl. Med. Mol. Imaging *44*, 850–857.

Yoshiyama, Y., Higuchi, M., Zhang, B., Huang, S.M., Iwata, N., Saido, T.C., Maeda, J., Suhara, T., Trojanowski, J.Q., and Lee, V.M. (2007). Synapse loss and microglial activation precede tangles in a P301S tauopathy mouse model. Neuron *53*, 337–351.

Zhang, W., Tarutani, A., Newell, K.L., Murzin, A.G., Matsubara, T., Falcon, B., Vidal, R., Garringer, H.J., Shi, Y., Ikeuchi, T., et al. (2020). Novel tau filament fold in corticobasal degeneration. Nature *580*, 283–287.

STAR★METHODS

KEY RESOURCES TABLE

REAGENT or RESOURCE	SOURCE	IDENTIFIER
Antibodies		
AT8	Endogen	Cat.#:MN1020; RRID:AB_223647
RD4	Upstate	Cat.#:05-804; RRID:AB_11211556
Chemicals, Peptides, and Recombinant Proteins		
^{18}F-PM-PBB3	this paper	N/A
^{11}C-PBB3	Maruyama et al., 2013	N/A
PBB5 (structurally identical to Styryl 7)	Sigma-Aldrich	Cat. #: 371823
BTA-1	Sigma-Aldrich	Cat. #: B9934
clorgiline	Sigma-Aldrich	Cat. #: M3778
selegiline	Sigma-Aldrich	Cat. #: NMID822
Sulforhodamine 101	Sigma-Aldrich	Cat. #: S7635
Experimental Models: Organisms/Strains		
Mouse:rTg4510:129S6.Cg-Tg(Camk2a-tTA)1Mmay/JlwsJ;FVB-Tg(tetO-MAPT*P301L)#Kha/JlwsJ	Santacruz et al., 2005	N/A
Mouse:PS19:B6;C3-Tg(Prnp-MAPT*P301S)PS19Vle/J	Yoshiyama et al., 2007	N/A
Experimental Models: Human Subjects		
Table S3 and see sections, "Clinical histories of autopsied patients" and "Clinical histories of patients with diverse FTLD spectrum and non-tauopathies"	this paper	N/A
Software and Algorithms		
Prism	Graph Pad	https://www.graphpad.com/scientific-software/prism/
SPSS	IBM	https://www.ibm.com/jp-ja/analytics/spss-statistics-software/
PMOD	PMOD Technologies Ltd	https://www.pmod.com/web/
Statistical Parametric Mapping software	The Wellcome Centre for Human Neuroimaging	https://www.fil.ion.ucl.ac.uk/spm/
MATLAB	MathWorks	https://www.mathworks.com/
Wake Forest University Pick atlas Tool	Wake Forest University	https://www.nitrc.org/projects/wfu_pickatlas/
FreeSurfer	Laboratory for Computational Neuroimaging	FreeSurfer http://surfer.nmr.mgh.harvard.edu
ImageJ	National Institutes of Health	https://imagej.nih.gov/ij/

RESOURCE AVAILABILITY

Lead Contact
Further information and requests for resources and reagents should be directed to the lead contact, Makoto Higuchi (higuchi.makoto@qst.go.jp)

Materials Availability
PM-PBB3 and its radiolabeling precursor will be made available on request. As PM-PBB3 and related materials are licensed to APRI-NOIA Therapeutics Inc., the material transfer will be subjected to a sublicense agreement with this company if there is potential for commercial application.

Data and Code Availability

The datasets supporting the current study have not been deposited in a public repository because they are related to clinical studies but are available from the Lead contact upon reasonable request.

EXPERIMENTAL MODEL AND SUBJECT DETAILS

Mice

The parental P301L tau responder line, parental tTA activator line, and the resultant F1 rTg4510 mice and littermates were generated and maintained as previously described (Ishikawa et al., 2018; Santacruz et al., 2005). PS19 tau transgenic mouse model of tauopathy was generated by using a cDNA construct of the human T34 tau (1N4R) with the P301S mutation in combination with a murine prion protein promoter (Yoshiyama et al., 2007). Six adult rTg4510 mice (two male, mean age 14.5 months; four female, mean age 8.9 months), six adult nTg wild-type (three male, mean age 12.9 months; three female, mean age 8.7 months), three adult PS19 mice (female, mean age 14 months), three adult wild-type mice (female, mean age 14 months) and four adult ddY mice (male, mean age 7 weeks) were used in this study. No sex- or gender-specific influence on the findings are to be expected, as rTg4510 and PS19 mice used in this study were mature ages of tau pathology in both males and females (Sahara et al., 2014; Yoshiyama et al., 2007); thus, the influence of sex and gender identity was not analyzed further. All mice studied here were maintained and handled in accordance with the National Research Council's Guide for the Care and Use of Laboratory Animals. Protocols for the present animal experiments were approved by the Animal Ethics Committees of the National Institutes for Quantum and Radiological Science and Technology. All procedures involving live mice received prior approval from the Institutional Animal Care and Use Committee of the University of Florida.

Human subjects

We included 23 HCs, 39 patients with diverse tauopathies - AD and FTLD spectrum and two non-tauopathies in the present study. All HCs (12 male, mean age 65.2 years) were without a history of neurologic and psychiatric disorders. Three MCI patients and 14 AD patients (seven male, mean age 70.7 years) met Petersen's criteria (Petersen et al., 1999) and NINDS-ADRDA criteria, respectively (McKhann et al., 1984). Eighteen PSP patients (12 male, mean age 71.2 years) were clinically diagnosed according to the Movement Disorder Society new diagnostic criteria (Höglinger et al., 2017) and classified into each clinical variant: 16 PSP-Richardson, one PSP-P and PSP-pure akinesia with gait freezing (PSP-PGF). Five other FTLD spectrums, two CBS, one PNFA and two bvFTD (one male, mean age 67.8 years), and two non-tauopathies; one Parkinson's disease (male, age 76 years) and one ALS (female, age 70 years), were also diagnosed according to each established criteria (Armstrong et al., 2013; Gorno-Tempini et al., 2011; Rascovsky et al., 2011). Demographic profiles of HCs, MCI/AD and PSP patients are summarized in Table S3; both genders were compared among the groups, and there was no significant difference between HCs and MCI/AD or PSP patients. Furthermore, detailed information of other patients is individually described in the following section.

In the present study, HCs and FTLD spectrum patients required PiB (-) to exclude preclinical and co-pathological AD, whereas MCI and AD patients needed PiB (+) by visual assessment of three raters, K.Tagai, Y.Takado and H.Shimada, according to the established criteria (Yamane et al., 2017). In addition, diagnoses of some patients were also validated according to their neuropathological examinations. One CBS patient was confirmed with CBD according to brain tissue biopsy before the PET scan (Arakawa et al., 2020); each of the PSP-Richardson and bvFTD patients was also neuropathologically diagnosed as PSP and PiD (Cairns et al., 2007) by autopsies after two years and one year after each PET scan, respectively.

Written informed consents were obtained from all subjects and/or from spouses or other close family members if subjects were cognitively impaired. This study was approved by the Radiation Drug Safety Committee and National Institutes for Quantum and Radiological Science and Technology Certified Review Board of Japan. The study was registered with UMIN Clinical Trials Registry (UMIN-CTR; number 000030248).

Clinical histories of autopsied patients

Brain autopsies were performed on two patients. The autopsy-confirmed PSP patient (65 years old, male) showed vertical supranuclear gaze palsy, a tendency to fall backward, progressive gait disturbance and mild decomposition/dysmetria in all extremities within 2 years. The diagnosis was PSP-Richardson according to the Movement Disorder Society new diagnostic criteria (Höglinger et al., 2017); meanwhile, the clinical features were also congruent with PSP with predominant cerebellar ataxia (PSP-C) (Kanazawa et al., 2009; Koga et al., 2016). He had undergone ^{18}F-PM-PBB3 imaging 2 years prior to death. Brain autopsy was performed at the National Hospital Organization Chiba-East-Hospital; the neuropathological diagnosis was definite PSP. The autopsy-confirmed PiD patient (60 years old) presented a six-year history of early behavioral disinhibition, stereotypical behavior and hyperorality, and was clinically diagnosed as bvFTD. The severely demented condition complicated detailed clinical assessment. On the other hand, obvious amyotrophy and pyramidal signs were not observed. He had undergone ^{18}F-PM-PBB3 imaging 1 year prior to death. Brain autopsy was performed at the National Hospital Organization Shimofusa Psychiatric Medical Center; the neuropathological diagnosis was PiD.

Clinical histories of patients with diverse FTLD spectrum and non-tauopathies

In addition, patients with diverse FTLD spectrum including PSP-P, PSP-PGF, CBS, and bvFTD were included in the present study. The PSP-P patient (62 years old, female) initially displayed features of Parkinson's disease, and thereafter showed PSP-related symptoms

within four years. The PSP-PGF patient (77 years old, male) presented with a five-year history of progressive gait instability and occasional falls and vertical supranuclear gaze palsy. Both patients with PSP variants also underwent single photon emission computed tomography (SPECT) imaging, which revealed decreased striatal dopamine transporter but also preserved the function of postganglionic cardiac sympathetic nerve endings. The CBS patient (65 years old, female) exhibited neurological symptoms including right-side dominant muscular rigidity, dystonia, gait disturbance and speech impairment. SPECT imaging showed left-side dominant decreased cerebral blood flow of frontal lobe and striatal dopamine transporter. The PNFA patient (75 years old, male) exhibited effortful speech and impaired comprehension of syntactically complex sentences compared to single-word comprehension. SPECT imaging showed left-side dominant posterior fronto-insular hypoperfusion. The bvFTD patient (72 years old, female) exhibited early behavioral disinhibition, stereotypical behavior and hyperorality. She was moderately demented (MMSE: 11, FAB: 2) and showed knife-blade brain atrophy in the frontal regions. The patient with clinically established Parkinson's disease (76 years old, male) exhibited right-dominant progressive parkinsonism (Hoehn & Yahr stage 3) and rapid eye movement sleep behavior disorder. Dopamine transporter SPECT imaging revealed a corresponding left-dominant decrease. The patient with probable ALS (70 years old, female) exhibited progressive muscle weakness in her extremities, slurred speech and difficulty swallowing in one year (ALS Functional Rating Scale-R: 26). Needle electrode examination revealed lower motor neuron degeneration, while brain MRI examination did not show obvious abnormal findings.

METHOD DETAILS

Compounds and Antibodies

PM-PBB3 1-fluoro-3-((2-((1*E*,3*E*)-4-(6-(methylamino)pyridine-3-yl)buta-1,3-dien-1-yl)benzo[*d*]thiazol-6-yl)oxy)propan-2-ol (Figure 1A) and tosylate precursor of ^{18}F-PM-PBB3 protected with tert-Butyloxycarbonyl group and 2-tetrahydropyranyl group (Figure S2) were custom-synthesized (Nard Institute). The precursor of ^{18}F-PM-PBB3 was also provided by APRINOIA Therapeutics Inc. PBB3 (2-((1*E*,3*E*)-4-(6-(methylamino)pyridine-3-yl)buta-1,3-dienyl)benzo[*d*]thiazol-6-ol) (Figure 1A) and desmethyl precursor of ^{11}C-PBB3 were also custom-synthesized (Nard Institute) (Maruyama et al., 2013). The reference standard for ^{11}C-PiB, 6-OH-BTA-1, is commercially available (ABX), and the desmethyl precursor of ^{11}C-PiB protected with methoxymethyl group, 6-MOMO-BTA-0, was custom-synthesized (KNC Laboratories). PBB5 (Maruyama et al., 2013), BTA-1, clorgiline and selegiline are commercially available (Sigma-Aldrich). A monoclonal antibody against tau phosphorylated at Ser 202 and Thr 205 (AT8, Endogen) and four-repeat tau isoform (RD4, Upstate) are commercially available.

Molecular Dynamics and MM/GBSA calculations
Structure preparation

The structure of Pick's disease (PiD) tau filaments (TAU^{PD}) was taken from the protein databank (PDB: 6GX5) (Falcon et al., 2018). The reported PiD tau assembly has three tau fibrils (K254–F378), so we prepared a five-fibril assembly by superimposing structures over each other to have a structure comparable to the one used in Tau^{AD} studies (Murugan et al., 2018). Five model compounds representing PET ligands AV-1451, MK-6240, PBB3, PM-PBB3, and THK-5351 were prepared using Maestro (Schrödinger, LLC). The structures of PET ligands were geometrically optimized initially by using the QM approach (HF/6-31+G(d,p) level of theory) and then further at B3LYP/6-31G*) in Gaussian 09, (Frisch et al., 2016). The RESP charges were calculated by *antechamber* of Amber18 using ESP potential from Gaussian.

Docking

Tau assembly was centered in the conformational search space of 30 Å × 30 Å × 70 Å. A large enough search space was chosen to ensure that all surface sites in the fibrils are captured. A total of 100 docking conformations of each PET ligands were obtained by software AutoDock Vina-carb using chi_coeff = 0 and chi_cutoff = 12. Used values of chi_coeff of and chi_cutoff switch Vina-carb to AutoDock Vina (Trott and Olson, 2010) therefore it is denoted as Vina throughout the manuscript. The exhaustiveness of 20 and energy range cutoff of 8 kcal·mol^{-1} was used. All the binding poses were further re-scored by re-scoring functions of X-Score (Wang et al., 2002). The docking population of PET ligands was calculated at each site, and all top-scoring docking poses from each cluster were further analyzed by extensive molecular dynamics (MD) simulations and binding free energy calculation techniques. Possible binding sites have been labeled as core site 1 (C1), and surface site 1 to 11 (S1 to S11).

MD Simulation

PiD tau assembly bound to PET ligand in all potential binding sites was prepared. For each binding site, the highest-scoring binding pose from each cluster was selected for MD simulation. The protein was treated with Amber ff14SB force field (Maier et al., 2015), whereas PET tracers were modeled using General Amber Force Field v.2.0 (GAFF2) (Wang et al., 2004) with RESP charges. All the complexes were solvated by the octahedral TIP3P water box extending 12 Å from each edge of the protein. A total of 45 Cl$^-$ ions were added to neutralize the whole system. A multi-step protocol published elsewhere (Nagae et al., 2017) was used to equilibrate complexes. Finally, a 100 ns MD of each complex was performed at NPT, using MD settings: the temperature at 300 K, temperature scaling by Langevin dynamics (collision frequency = 2), pressure relaxation every 1.2 picoseconds, SHAKE constraints, nonbonded interaction cutoff of 10 Å, and 2 fs integration time step.

MM/GBSA Calculations

To calculate binding free energy of the ligand in each site, solvent molecules and ligands present in remaining binding sites were removed from the trajectory. A total of 1000 snapshots extracted after every 10 ps from a 100 ns MD simulation were extracted

and used for binding energy calculation. Then the binding energies of the PET tracer were calculated using the MM/GBSA approach as used elsewhere (Mishra and Koča, 2018). A similar procedure was repeated for the PET ligand in other binding sites one by one. The GB^{OBC} generalized-born model (Okamoto, 2004) was used with the mbondi2 radii set. Salt concentration was set to 0.15 M. The surface tension and non-polar solvation free energy correction terms were set to 0.005 kcal·mol^{-1} and 0.0, respectively, for solvent accessible surface area (SASA) calculation. An offset value of 0.0 was used to correct non-polar solvation free energy contribution. The interior and exterior dielectric constants were set to 1 and 80, respectively. Other parameters were set to their default values in Amber18.

Radiosynthesis
^{11}C-PBB3 was radiosynthesized using its desmethyl precursor, according to the method previously described (Maruyama et al., 2013). Radiolabeling of ^{18}F-PM-PBB3 was performed as the synthetic pathway described in Figure S1. Tosylate precursor of ^{18}F-PM-PBB3 was reacted with ^{18}F-fluoride in the presence of dimethyl sulfoxide, K_2CO_3 and K222 at 110°C for 15 min. After cooling the reaction vessel to 90°C, hydrochloric acid was added to the mixture and maintained for 10 min to delete the protecting groups. Sodium acetate was added to the reaction vessel, and the radioactive mixture was transferred into a reservoir for high-performance liquid chromatography (HPLC) purification (Waters Atlantis prep T3 column, 10 × 150 mm; CH_3CN/50 mM AcONH$_4$ = 4/6, 5 ml/min). The fraction corresponding to ^{18}F-PM-PBB3 was collected in a flask containing 25% ascorbic acid solution and Tween 80, and was evaporated to dryness under a vacuum. The residue was dissolved in 17 mL of saline (pH 7.4) to obtain ^{18}F-PM-PBB3 as an injectable solution. The final formulated product was radiochemically pure ($\geq$95%) as detected by analytic HPLC (Waters Atlantis prep T3 column, 4.6 × 150 mm; CH_3CN/50 mM AcONH$_4$ = 4/6, 1 ml/min). The specific activity of ^{18}F-PM-PBB3 at the end of synthesis was 58-761 GBq/μmol, and ^{18}F-PM-PBB3 maintained its radioactive purity exceeding 90% for over 3 hr after formulation. Radiolabelling of ^{11}C-PiB was performed as previously described (Maeda et al., 2011).

PBB3 is known to undergo photo-isomerization under ordinary fluorescent light (Hashimoto et al., 2014). ^{18}F-PM-PBB3 and ^{11}C-PBB3 in a colorless vial were isomerized by exposure to fluorescent light for 30 min (Figures S12A and S12B, left). UV-VIS absorption spectra for PM-PBB3 and PBB3 indicated that these compounds do not absorb light with a wavelength longer than 500 nm (Figure S12C). Then, ^{18}F-PM-PBB3 and ^{11}C-PBB3 in a colorless vial were placed under a UV-cut light (< 500 nm wavelength cutoff, ECO-HiLUX HES-YF, 2200 lm, Iris Oyama Inc.) for 30 min, and both compounds were found to be stable under this condition (Figures S12A and S12B, right). Based on these results, radiosyntheses of ^{18}F-PM-PBB3 and ^{11}C-PBB3 and all experiments with these compounds were performed under UV-cut light to avoid photo-isomerization of these compounds.

Stability of ^{18}F-PM-PBB3 and ^{11}C-PBB3 under UV-cut condition
^{18}F-PM-PBB3 and ^{11}C-PBB3 in a colorless vial were exposed to the ordinary fluorescent light or UV-cut light for 30 min (1 m from the lighting source). Analytic HPLC was conducted using a HPLC system consisting of a pump (PU-2089, JASCO Corporation), a diode array detector (MD-2015, JASCO Corporation), a Rheodyne manual injector (IDEX Health & Science LLC) with a 20 μl loop, and a NaI(Tl) scintillation detector with an ACE Mate Amplifier and BIAS supply (925-SCINT, ORTEC, Oak Ridge) for radioactivity detection. Data acquisition and interpretation were performed with ChromNAV (ver. 1.5.2.0, JASCO Corporation). The radiochromatograms were corrected for decay. YMC-Triart PFP analytical columns were used with a mobile phase consisting of a mixture of acetonitrile and 0.1% formic acid (1/1 for ^{18}F-PM-PBB3 with 2 ml/min flow rate; 4/6 for ^{11}C-PBB3 with 1 ml/min flow rate). The UV-VIS absorption spectra of PM-PBB3 and PBB3 were measured under the HPLC condition.

Postmortem brain tissues
Postmortem human brains were obtained from autopsies carried out at the Center for Neurodegenerative Disease Research of the University of Pennsylvania Perelman School of Medicine on patients with AD, PiD, PSP and CBD, and at the Department of Neurology at the Chiba-East National Hospital on patients with PSP. Tissues for homogenate binding assays were frozen, and tissues for histochemical, immunohistochemical and autoradiographic labeling were frozen or fixed in 10% neutral buffered formalin followed by embedding in paraffin blocks.

Neuropathologic assessment
Formalin-fixed brains underwent systematic and standardized sampling with neuropathologic evaluation by experienced neuropathologists. Brain slices were immunostained for tau pathology, Aβ plaques, α-synuclein pathology and TDP-43 pathology with antibodies that are made freely available to all Alzheimer's disease centers or are commercially available as described previously (Robinson et al., 2011; Takeda et al., 2009). Braak neurofibrillary tangle stage, Thal amyloid phase and CERAD score were assigned by microscopic examinations of sections according to published criteria (Boluda et al., 2014; Braak and Braak, 1991; Thal et al., 2002). Presence of other co-morbid pathologies (vascular disease, Lewy bodies, TDP-43 inclusions, argyrophilic grains and hippocampal sclerosis) were also assessed for each slide as described previously (Robinson et al., 2018).

In vitro binding assay
Frozen tissues derived from the frontal cortex of an AD patient, the motor cortex of a PSP patient, and the forebrains of Tg and nTg mice were homogenized in 50 mM Tris-HCl buffer, pH 7.4, containing protease inhibitor cocktail (cOmplete^{TM}, EDTA-free, Roche),

and stored at −80°C pending analyses. To assay radioligand binding with homologous or heterologous blockade, these homogenates (100 μg tissue) were incubated with 1 nM ^{18}F-PM-PBB3 (specific radioactivity: 257.2 ± 22.2 GBq/μmol) in the presence or absence of non-radiolabeled PM-PBB3, BTA-1, clorgiline and selegiline at varying concentrations ranging from 10^{-11}-10^{-6} M in Tris-HCl buffer containing 10% ethanol, pH 7.4, for 30 min at room temperature. Non-specific binding of ^{18}F-PM-PBB3 was determined in the presence of 5×10^{-7} M PM-PBB3. To assay radioligand binding with a homologous blockade, Tg mouse forebrain homogenates (100 μg tissue) were incubated with 5 nM ^{11}C-PBB3 (specific radioactivity: 51.6 GBq/μmol) in the presence or absence of non-radiolabeled PBB3 at varying concentrations ranging from 10^{-11}-10^{-6} M in Tris-HCl buffer containing 10% ethanol, pH 7.4, for 30 min at room temperature. Non-specific binding of ^{11}C-PBB3 was determined in the presence of 5×10^{-7} M PBB3. Samples were run in quadruplicates and specific radioligand binding was determined as pmol/g tissue. Ki was determined by using non-linear regression to fit a concentration-binding plot to one-site binding models derived from the Cheng-Prusoff equation with GraphPad Prism version 5.0 (GraphPad Software), followed by F-test for model selection. Kd and Bmax were calculated from homologous competitive binding using this function:

$$Kd = Ki = IC50 - [Radioligand]$$

$$Bmax = \frac{Top - Bottom}{[Radioligand]/(Kd + [Radioligand])}$$

where IC_{50} and [Radioligand] are concentrations of the competitor inducing 50% inhibition and radiotracer concentration, respectively, and Top and Bottom are upper and lower plateaus of the plot curve, respectively.

In vitro and *ex vivo* autoradiography

In vitro autoradiography was performed using 6-μm-thick deparaffinized sections derived from AD and 20-μm-thick fresh frozen sections post-fixed in 4% paraformaldehyde solution derived from PSP brains. For labeling with ^{18}F-PM-PBB3, sections were pre-incubated in 50 mM Tris-HCl buffer, pH 7.4, containing 20% ethanol at room temperature for 30 min, and incubated in 50 mM Tris-HCl buffer, pH 7.4, containing 20% ethanol and 5 nM of ^{18}F-PM-PBB3 (specific radioactivity: 58 GBq/μmol) at room temperature for 60 min. The samples were then rinsed with ice-cold Tris-HCl buffer containing 20% ethanol twice for 2 min each, and dipped into ice-cold water for 10 s. For *ex vivo* autoradiography, Tg and nTg wild-type at 9.7 months of age and PS19 and wild-type at 14 months of age were anesthetized with 1.5% (v/v) isoflurane and given 28.7 ± 4.6 MBq ^{18}F-PM-PBB3 by syringe via tail vein. The animals were sacrificed by decapitation at 30 min (Tg and nTg mice) or 20 min (PS19 and wild-type mice) after tracer administration. Brains were harvested and cut into 20-μm-thick sections on a cryostat (HM560; Thermo Fisher Scientific).

The sections labeled with ^{18}F-PM-PBB3 were subsequently dried by treating with warm air, and were then exposed to an imaging plate (BAS-MS2025, Fuji Film). The imaging plate was scanned with a BAS-5000 system (Fuji Film) to acquire autoradiograms. Fresh frozen sections generated in the process of *ex vivo* autoradiography were post-fixed in 4% paraformaldehyde solution for the subsequent histological examination.

Histological examination

For fluorescence labeling, deparaffinized sections and sections used for autoradiography were incubated in 50% ethanol containing 25 μM of non-radiolabeled PM-PBB3 at room temperature for 30 min. The samples were rinsed with 50% ethanol for 5 min, dipped into distilled water twice for 3 min, and mounted in non-fluorescent mounting media (VECTASHIELD, Vector Laboratories). Fluorescence images were captured using a DM4000 microscope (Leica) equipped with a custom filter cube for PBB3 (excitation band-pass at 414/46 nm and suppression low-pass with 458 nm cutoff) (Ono et al., 2017). Following microscopy, sections were autoclaved for antigen retrieval, and immunostained with AT8. Immunolabeling was then examined using DM4000. Finally, the tested samples were used for GB staining with Nuclear Fast Red (Sigma-Aldrich) counter-staining after pretreatment with 0.25% $KMnO_4$ followed by 2% oxalic acid.

In vivo two-photon fluorescence microscopy

Two weeks before the measurement, surgery to create cranial windows was performed. For this procedure, the animals were anesthetized with a mixture of air, oxygen, and isoflurane (3%–5% for induction and 2% for surgery) via a facemask, and a cranial window (3-4 mm in diameter) was attached over the left somatosensory cortex, centered at 1.8 mm caudal and 2.5 mm lateral from the bregma, according to the 'Seylaz-Tomita method' (Tomita et al., 2005). A custom metal plate was affixed to the skull with a 7-mm-diameter hole centered over the cranial window.

Sulforhodamine 101 (Sigma-Aldrich) dissolved in saline (10 mM) was injected intraperitoneally (8 μl/g body weight) just before initiation of the imaging experiments. The awake animals were placed on a custom-made apparatus, and real-time imaging was conducted by two-photon laser-scanning microscopy (TCS-SP5 MP, Leica) with an excitation wavelength of 900 nm. Two-photon imaging was performed before and 5, 30, 60, 90 and 120 min after intravenous injection of 0.05 mg of PM-PBB3 and PBB3 dissolved in dimethyl sulfoxide: saline = 1: 1 (0.05% W/V). An emission signal was separated by a beam splitter (560/10 nm) and simultaneously

detected through a band-pass filter for sulforhodamine 101 (610/75 nm) and PM-PBB3 and PBB3 (525/500 nm). A single image plane consisted of 1024 by 1024 pixels, and in-plane pixel-size was 0.25–0.45μm depending on an instrumental zoom factor. Images were acquired at a depth of 0.2–0.4 mm from the cortical surface. In each of the resulting images from Tg mouse, fluorescence intensity from 10 randomly selected fluorescence-labeled pathologies was measured by ImageJ, and the average was calculated after background normalization. It should be noted that the background intensity of each image was acquired by averaging the fluorescence intensity at 10 randomly selected areas where no fluorescence-labeled pathologies were found.

In vivo PET imaging in mice

PET scans were performed using a microPET Focus 220 animal scanner (Siemens Healthcare) providing 95 transaxial slices 2.0 mm (center-to-center) apart, a 19.0-cm transaxial field of view (FOV), and a 7.6-cm axial FOV. Prior to the scans, Tg and nTg mice at 8-9 months of age (n = 3 each) and PS19 mouse at 14 months of age were anesthetized with 1.5% (v/v) isoflurane. Emission scans were carried out for 90 min (^{18}F-PM-PBB3) or 60 min (^{11}C-PBB3) in 3D list mode with an energy window of 350-750 keV, immediately after intravenous injection of ^{18}F-PM-PBB3 (28.3 ± 10.3 MBq) or ^{11}C-PBB3 (29.7 ± 9.3 MBq). All list-mode data were sorted into 3D sinograms, which were then Fourier-rebinned into 2D sinograms (frames for ^{18}F-PM-PBB3: 4 × 1, 8 × 2, and 14 × 5 min, frames for ^{11}C-PBB3: 10 × 1, 6 × 5, and 2 × 10 min). Average images were generated with maximum *a posteriori* reconstruction, and dynamic images were reconstructed with filtered backprojection using a 0.5-mm Hanning filter. VOIs of hippocampus and cerebellum were placed using PMOD image analysis software (PMOD Technologies Ltd) with reference to the individual MR images.

Radiometabolite analysis in mice

^{18}F-PM-PBB3 (31 MBq/150 pmol/0.3 mL) was intravenously applied to 7-week-old male ddY mice under anesthesia (isoflurane airflow, 1.5% (v/v)). Mice were decapitalized at corresponding time points (1 and 5 min after ^{18}F-PM-PBB3 application), respectively, and blood and brain samples were collected accordingly. For blood samples, after centrifugation at 13,000 g for 3 min at 4°C, the resulting plasma was then deproteinized by adding the same amount of acetonitrile, and the plasma sample was collected for HPLC analysis. For brain samples, the hemisphere of the brain was homogenized in ice-cold saline (twice volume of its wet weight). After deproteinization by adding the same amount of acetonitrile and centrifugation at 20,000 g for 2 min at 4°C, the supernatant of each brain homogenate was subjected to HPLC analysis. The plasma and brain samples were analyzed by HPLC using columns (YMC-Triart C18 ExRS (5 μm, 10 mm i.d. × 10 mm, YMC) and YMC-Triart C18 ExRS (5 μm, 10 mm i.d. × 150 mm, YMC)) and a detection system (ultraviolet detector: UV-2075, NaI(TI) scintillation detector: S-2493A) with a mobile phase consisting of 90% acetonitrile/ 0.1 mol/L ammonium acetate = 0/100 (0-3 min); 60/40 (3-12 min); 90/10 (12 min-) at a flow rate of 4 ml/min. Radio-metabolite analysis of ^{11}C-PBB3 in mice was performed as described previously (Hashimoto et al., 2014).

Tissue extraction and immunoblot analyses

PS19 and wild-type mice were intraperitoneally anesthetized with 20 mg/kg sodium pentobarbital (Somnopentyl, Kyoritsu Seiyaku, Japan) and brains were removed after perfusion with saline. Brainstem and hippocampus were separated and store at −80°C pending analyses. Frozen brain tissues were homogenized in 50 nM Tris-HCl (containing 0.1% protease inhibitor mixture and 0.5 mM PMSF, pH 7.4, 4°C). The protein amounts of the homogenates were determined by Lowry protein assay, and samples were diluted to 5 mg protein in 1 mL of homogenate buffer. A part of the suspension was added to the equivalent amount of homogenate buffer containing 1% Triton X-100 and mixed well. The sample was centrifuged at 15,000 × g for 10 min at 4°C. Supernatants were collected (Triton X-100-soluble fraction), and the resultant pellets were resuspended in homogenate buffer (Triton X-100-insoluble fraction). Triton X-100-soluble and –insoluble fractions corresponding to 12.5 μg protein were applied to a Sodium Dodecyl Sulfate (SDS) polyacrylamide gel. After electrophoresis and transfer of proteins to a polyvinylidene fluoride membrane (Immobilon-P, Millipore, USA), the membrane was immersed in Tris-buffered saline (TBS) containing 0.05% Tween 20 and 3% bovine serum albumin (BSA), and then reacted for 1 h with AT8 in TBS containing 0.05% Tween 20 and 3% BSA. The primary antibody was detected by HRP-conjugated anti-IgG antibody and enhanced chemiluminescence method. The signals obtained with primary antibody were measured using image quantification software (Quantity One, Bio-Rad Laboratories, USA) based on the immunoblot images.

In vivo MRI and PET Imaging in Human Subjects

MR images were acquired with a 3-T scanner, MAGNETOM Verio (Siemens Healthcare). Three-dimensional volumetric acquisition of a T1-weighted gradient echo sequence produced a gapless series of thin sagittal sections (TE = 1.95 ms, TR = 2300 ms, TI = 900 ms, flip angle = 9°, acquisition matrix = 256 × 256 × 250, voxel size = 1 × 1 × 1mm). PET assays were conducted with a Biograph mCT flow system (Siemens Healthcare), which provides 109 sections with an axial field of view of 16.2 cm. The intrinsic spatial resolution was 5.9 mm in-plane and 5.5 mm full-width at half-maximum axially. Images were reconstructed using a filtered back projection algorithm with a Hanning filter (4.0 mm full-width at half-maximum).

^{18}F-PMPBB3 had an average injected dose of 189.5 ± 22.5 MBq with molar activity at the time of injection of 238.5 ± 71.8 GBq/ μmol. ^{18}F-PM-PBB3 PET scans were performed with two steps of scan protocol. In the first protocol, dynamic PET scans with arterial blood sampling were performed with two imaging sessions of 60 min each with a 30-min break between sessions (0–60 and 90-150 min). The dynamic scan consisted of 12 × 10 s, 2 × 30 s, 7 × 1 min, 1 × 2 min, 1 × 3 min, 3 × 5 min, 3 × 10 min for the initial

60-min session, and 6 × 10-min frames for the second 60-min session. In the second protocol, a 20-min PET acquisition was performed 90 min after injections (4 × 5-min frames) (also see Supplemental Information).

^{11}C-PBB3 and ^{11}C-PiB PET scans were performed following a previously reported protocol (Kimura et al., 2015; Maruyama et al., 2013; Shimada et al., 2016). Seventy-minute dynamic PET scans were performed after an intravenous injection of ^{11}C-PBB3 (injected dose: 423.1 ± 57.2 MBq, molar activity: 70.0 ± 18.6 GBq/ μmol). ^{11}C-PiB (injected dose: 521.2 ± 87.3 MBq, molar activity: 81.8 ± 40.5 GBq/ μmol) PET scan was conducted with a 20-min acquisition 50 min after injections; a ECAT EXACT HR+ scanner (CTI PET Systems, Inc.) was also utilized for ^{11}C-PiB alternatively.

Radiometabolite analysis in human subjects

Arterial blood sampling was performed manually. To determine the unmetabolized ^{18}F-PM-PBB3 fraction in plasma, blood samples (1.5 mL each) taken at 3, 10, 20, 30, 60, 90, and 150 min were subjected to metabolite analysis by high performance liquid radiochromatography. An aliquot of 0.7 mL plasma was mixed with the same amount of acetonitrile and centrifuged at 13,000 g at 4°C for 2 min for deproteinization. Then an aliquot of the supernatant was injected into a reverse-phase HPLC system (JASCO Corporation). The columns used were YMC-Triart C18 ExRS (5 μm, 10 mm i.d. × 10 mm, YMC) and YMC-Triart C18 ExRS (5 μm, 10 mm i.d. × 150 mm, YMC), respectively. The mobile phase was acetonitrile/100 mM ammonium acetate solution (50/50) at an isocratic condition, and the flow rate was 4.0 mL/min. Effluent radioactivity was detected with a home-made NaI (Tl) scintillation detector system (Takei et al., 2001). The retention time of the radiochromatography peak of ^{18}F-PM-PBB3 was identified by the optical absorption of standard PM-PBB3 at a detection wavelength of 390 nm. The unmetabolized fraction was calculated as the peak area ratio of unmetabolized ^{18}F-PM-PBB3 to the total peaks detected. Radiometabolite analysis of ^{11}C-PBB3 in human subjects was performed as described previously (Kimura et al., 2015).

Image analyses in Human Subjects
Data preprocessing

Data preprocessing was performed using PMOD 3.8 and Statistical Parametric Mapping software (SPM12, Wellcome Department of Cognitive Neurology). Acquired PET images were rigidly coregistered to individual T1-weighted MR images. SUVR images were generated from averaged PET images at the following intervals: 30-50 min (^{11}C-PBB3), 50-70 min (^{11}C-PiB) and 90-110 min (^{18}F-PM-PBB3) post injection, respectively. Cerebellar gray matter was used as reference region. Regarding VOI analyses, surface-based cortical reconstruction was conducted with FreeSurfer 6.0 (http://surfer.nmr.mgh.harvard.edu/) from the Desikan–Killiany–Tourville atlas (Klein and Tourville, 2012), and then cortical and Braak-staging VOIs were generated. Subcortical VOIs were transformed from a template atlas (Talairach Daemon atlas from the Wake Forest University PickAtlas version 3.0.5) to each native space using the deformation field obtained from the tissue-class segmentation of SPM12. Regarding voxel-wise analysis, each image was spatially normalized to MNI (Montreal Neurologic Institute) space using Diffeomorphic Anatomical Registration Through Exponentiated Lie Algebra (DARTEL) algorithm. Subsequently, normalized images were smoothed with a Gaussian kernel at 8-mm full-width at half-maximum. Partial volume correction was not performed in the present study.

Characteristics of ^{18}F-PM-PBB3 in Human Subjects

We explored uptake into the brain, and the dynamic range and distribution of specific binding of ^{18}F-PM-PBB3. A head-to-head comparison of ^{18}F-PM-PBB3, ^{11}C-PBB3 and ^{11}C-PiB was conducted in the same individuals. Regional time-activity curves as standardized uptake value (SUV) and SUVR were generated over the time course of the dynamic scan; in addition, linear regression analyses were performed among the regional SUVR of each tracer derived from the same subjects. For AD, VOIs were set in each lobe of the cerebral cortex to compare the dynamic range and distribution of specific binding among the three tracers. For PSP, the same number of VOIs as for AD were set to compare the dynamic range among PBB3 compounds in the subcortical structures where PSP is considered to show moderate to high tau burden (Hauw et al., 1994) - globus pallidus, substantia nigra, red nucleus, and subthalamic nucleus. Besides, the midbrain was also used as a broad target-region for PSP.

Full kinetic analysis in human subjects

Four HCs, one MCI, two AD, and two PSP (PSP-Richardson [autopsy-confirmed] and PSP-PGF) patients who underwent arterial blood sampling were included in the analysis; the MCI and AD patients were treated as AD group. First, the total distribution volume (V_T) was determined by compartment model analyses and a multilinear analysis using a metabolite-corrected plasma input function. For the compartment model analyses, the standard one- and two-tissue compartment models (1TCM and 2TCM) were applied with relative weighting by frame duration in each region. For the multilinear analysis, multilinear analysis 1 (MA1) (Ichise et al., 2002) was performed with t* = 40. Parameter identifiability (Akaike, 1973) of V_T and visual assessment were used to choose a model with better fitting. Furthermore, we examined V_T value changing by shortening data duration from 150 min to 90 min in the temporal cortex where tau aggregation is stereotypically seen in AD. Ultimately, we chose the one showing stable estimations as the appropriate kinetic model.

Second, we tested the feasibility of SUVR obtained from a short scan duration (20 min) in HCs and AD patients. An optimal scan time window was selected as SUVR equivalent to DVR obtained from 150-min scan duration in the temporal cortex. SUVR values were obtained for the following intervals: 40–60, 90–110, 100–120, 110–130, 120–140, and 130–150 min post-injection. DVR was calculated from V_T / V_{ND}, where V_{ND} is the nondisplaceable volume of distribution, V_T in the cerebellar cortex. Each V_T value was

estimated from the appropriate kinetic model. Furthermore, the selected scan time window of SUVR was also applied to the PSP patients. These comparisons were performed by calculating Pearson correlation coefficients.

Third, we investigated K_1 bias using a simple simulation of 2TCM. The parameters K_1 and k2 in 2TCM are tracer uptake and washout rates between blood and brain, which are considered to be affected by the alteration of CBF, particularly by aging and disease progression. Therefore, we evaluated the impact of K_1 changes on time-activity curves (TACs) with a simple simulation using kinetic parameters obtained with 2TCM in this study. A set of estimated kinetic parameters (K_1-k4) of the temporal (target region) and cerebellar (reference region) cortices of a mild AD patient and metabolite-corrected input function was used. K_1 values were assumed to be 20% reduced and 10% increased respectively.

Assessing Tau Deposits Associated with AD

Progressions of tau deposits in HCs, MCI and AD patients were evaluated according to the image-based tau stage. We calculated SUVRs and Z scores of composite VOIs based on Braak's pathological stages of neurofibrillary tangle: stages I/II(transentorhinal), III/IV (limbic) and V/VI (neocortical) (Cho et al., 2016; Schöll et al., 2016). Hippocampus was excluded from the analysis because of contamination of the signal from off-target binding in the choroid plexus. The stage showing highest regional Z score > 2.5 was assigned to the individual image-based tau stage: subjects showing lack of involvement of stages I/II were classified as stage zero. Subsequently, we assessed distribution of tau deposits and clinical association in each image-based tau stage. Voxel-level comparisons were performed comparing stages I/II, III/IV and V/VI to stage zero. Group comparisons between MCI/AD patients and HCs were also performed in each VOI; in addition, regression analyses between SUVR of each VOI and CDRSoB were also performed in MCI and AD patients.

Assessing Tau Deposits Associated with PSP-Richardson

Associations among tau deposits, clinical symptoms and brain atrophy were assessed. Brain atrophy was estimated by voxel-based morphometry. Voxel-level comparisons between PSP-Richardson patients and HCs were performed regarding distributions of tau deposits and brain atrophy. Group comparisons using subcortical VOIs were also conducted; in addition, regression analyses between SUVR of each VOI and PSPRS scores were also performed in PSP-Richardson patients.

QUANTIFICATION AND STATISTICAL ANALYSIS

Statistical calculations with respect to VOI analyses were performed using GraphPad Prism 7.0 and SPSS 24. Group comparisons of SUVR values derived from VOIs between HCs and MCI/AD or PSP-Richardson groups were conducted by two-sample t test; gender differences were evaluated by Fisher exact test. Pearson correlation and linear regression analyses were conducted in a head-to-head comparison among the respective tracers. Clinical associations were also explored by Pearson correlation analysis. Furthermore, ROC curve analyses were performed to generate area under the curve (AUC) values (MCI/AD versus HCs and PSP versus HCs); we selected optimal thresholds maximizing sensitivity+specificity in each comparison. For the analyses, the V/VI and STN VOIs were chosen, as the SUVR values of these VOIs were significantly correlated with disease severity.

Voxel-wise analyses were conducted by SPM12; we used the two-sample t test model of SPM12 for group comparisons. The extent threshold was set to the expected voxels per cluster. For multiple voxel comparisons, family-wise error corrections at cluster levels were applied (p < 0.05). Data in figures represent mean ± SD, with sample size in figure legends and detailed statistic values listed in Results.